Environmental Impact Assessment Review 97 (2022) 106914

Contents lists available at ScienceDirect

Environmental Impact Assessment Review

journal homepage: www.elsevier.com/locate/eiar

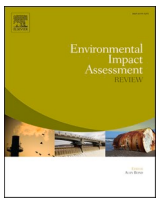

Research on the optimized environment of large bridges based on multi-constraint coupling

Zhi Wu Zhou *, Julián Alcalá, Víctor Yepes

Institute of Concrete Science and Technology (ICITECH), Universitat Politècnica de València, 46022 València, Spain

ARTICLE INFO

Keywords:
Construction industry
Structure model
Topology optimization
Load
Sustainable
Design

ABSTRACT

To reduce the pollution emissions of bridges to the environment, researchers need to conduct more in-depth research and design the structure. Today's architectural, structural, and mechanical engineers pay more attention to funders' requirements and pursue the maximization of economic benefits. The research begins with establishing a theoretical model of the bridge's robustness under dead and dynamic loads: applying a Three-Dimensional (3D) solid finite element model, swarm intelligence optimization algorithm, and mathematical model of quadratic interpolation approximation solves the problems of multiple loads, discrete data, and convergence. Based on the establishment and analysis data of the research model, the research and analysis of the optimal topology bridge model are completed, and the optimal structure size is obtained. The carbon emissions from the bridge optimization decreased by 2242.92 t, accounting for 25% of the total emissions. This data is shocking, and it also gives investors and governments a painful reminder that they must pay more attention to the sustainable construction and development of the construction industry and achieve the goal of zero carbon emissions in the construction industry as soon as possible.

1. Introduction

In October 2018, a United Nations report concluded that carbon dioxide emissions from fossil fuels, construction, aviation, and agribusiness continued to rise. The planet could warm by four °C by the end of the century. Data from the International Energy Agency at the end of 2019 showed that global atmospheric carbon dioxide emissions were 33 billion tonnes (t) (Semenova, 2020).

Building energy consumption reaches 25% of the total global energy consumption. Building energy in developing countries has increased to 40%; carbon dioxide has risen to 30%. Specifically, 15% of the emissions are generated from the construction stage and 21% from the required transport (Bajželj et al., 2013). Previous research data on bridge environments show that carbon emissions are generated from transportation (Pons et al., 2018; Zhou et al., 2020a). The key is thus to reduce the pollution from the transport sector.

In the face of the constant high pollution and energy consumption in the building industry, it is essential to realize sustainable development and solve the problems of environmental pollution and excessive energy consumption (Tsai et al., 2011).

1.1. Sustainable development

Sustainable bridge research minimizes costs and adverse environmental and social impacts. Therefore, the optimal design has become an important research method for sustainable development assessment. Scopus is used as the retrieval software in this study to select key search terms of high quality (Malhotra et al., 2017). As a result, the three terms 'Environment,' 'Sustainable development,' and 'Building industry' are included in the literature retrieval (Secundo et al., 2020), and the period from 2000 to 2021 is determined as the selection range. A total of 2635 papers are retrieved, and then 270 papers are filtered by entering the terms 'Sustainability' and 'Optimization.' Through literature research, it was found that the three pillars of sustainability indicators are still environmental, economic, and social impacts. Sustainable research in the construction industry accounted for >67.5% (Paya-Zaforteza et al., 2010). Environmental control models include recycling, reducing waste and pollution, and protecting natural resources. The scope of research is expanding, and research in the field of perfecting large-scale solid bridges needs to be strengthened. (Aigbavboa et al., 2017).

This paper task is to build a 3D solid model using Abaqus, conduct a highly detailed analysis of the structural stress and energy on the bridge

* Corresponding author.
E-mail address: zhizh2@doctor.upv.es (Z.W. Zhou).

https://doi.org/10.1016/j.eiar.2022.106914
Received 17 May 2022; Received in revised form 13 August 2022; Accepted 9 September 2022
Available online 21 September 2022
0195-9255/© 2023 The Authors. Published by Elsevier Inc. This is an open access article under the CC BY-NC-ND license (http://creativecommons.org/licenses/by-nc-nd/4.0/).

structure, and impose constraints after gaining data. Afterward, Topology optimization (TO) is carried out several times to redesign the structural components. The curve fitting method of swarm intelligence optimization advanced mathematics is used to approximate the scientific calculation method, and the calculation program is compiled to refit the structural stress. After many iterations, the optimal models that minimize material, energy consumption, and environmental pollution is found.

1.2. Optimization of bridge

Kristine Ek et al. (Ek et al., 2020) studied that early-stage control of planning and design is an effective measure to improve the sustainability of bridges. Ignacio J applied multi-objective optimization to find designs with lower cost, longer corrosion initiation time, and higher safety; This is also one of the strategies to reduce environmental pollution (García-Segura et al., 2017). Penadés-Plà et al. (Penadés-Plà et al., 2020) the evaluation of three prestressed concrete bridges found that the most significant environmental impact indicators were concrete, steel, and diesel consumption. The abovementioned studies prove that the optimal design for concrete and steel bars in the bridge structure can reduce environmental pollution (optimization of redundant structures of bridges, under the condition of ensuring quality and safety).

1.3. Concept of TO

Under the circumstance that the bridge structure meets the criteria for rigidity, strength, and durability, structural optimization will effectively improve the members' sustainability (Allaire et al., 2004). TO is one of the three sub-fields of structural optimization, and the others are size and shape optimization. TO is used in the early design stage of the structure. Its principle is to reduce the structural weight by realising the optimal material distribution, combining and eliminating unnecessary systems (Zhang and Sun, 2006). Taking TO as the modeling framework and this paper aims to optimise and eliminate redundant bridge structures, reduce the consumption of concrete and steel bars, and ultimately achieve sustainability of the bridge.

Purposes of this paper: To carry out the in-depth design of bridge structures two and multiple times; reassess the environmental impact of the bridge using Abaqus CAE (CAE is format file) 6.14 and Open LCA (Life Cycle Assessment) 1.10.3 based on the in-depth analysis of the design process; and minimize the structural weight and materials consumption under the premise of satisfying safety and quality requirements, thus achieving the carbon emissions target.

Innovations of this paper:

(1) This work overcomes many difficulties in establishing finite element models of statically indeterminate structures (for example, a wide variety of components, huge structural dimensions, large slenderness ratios of rods, etc). Finally, model meshing paradigms had been established through fine segmentation of component and assembly designs.
(2) This work uses a 3D study optimization model from start to finish, clearly demonstrating the robustness analysis process of each group of study components and the internal microcell structure. It fills and enriches the gaps in research models and methodologies in this field. It expands the research ideas in this field from macro theory to the micro world.
(3) The research has proved that there are certain defects in the design code and building code of Chinese bridges. Architectural

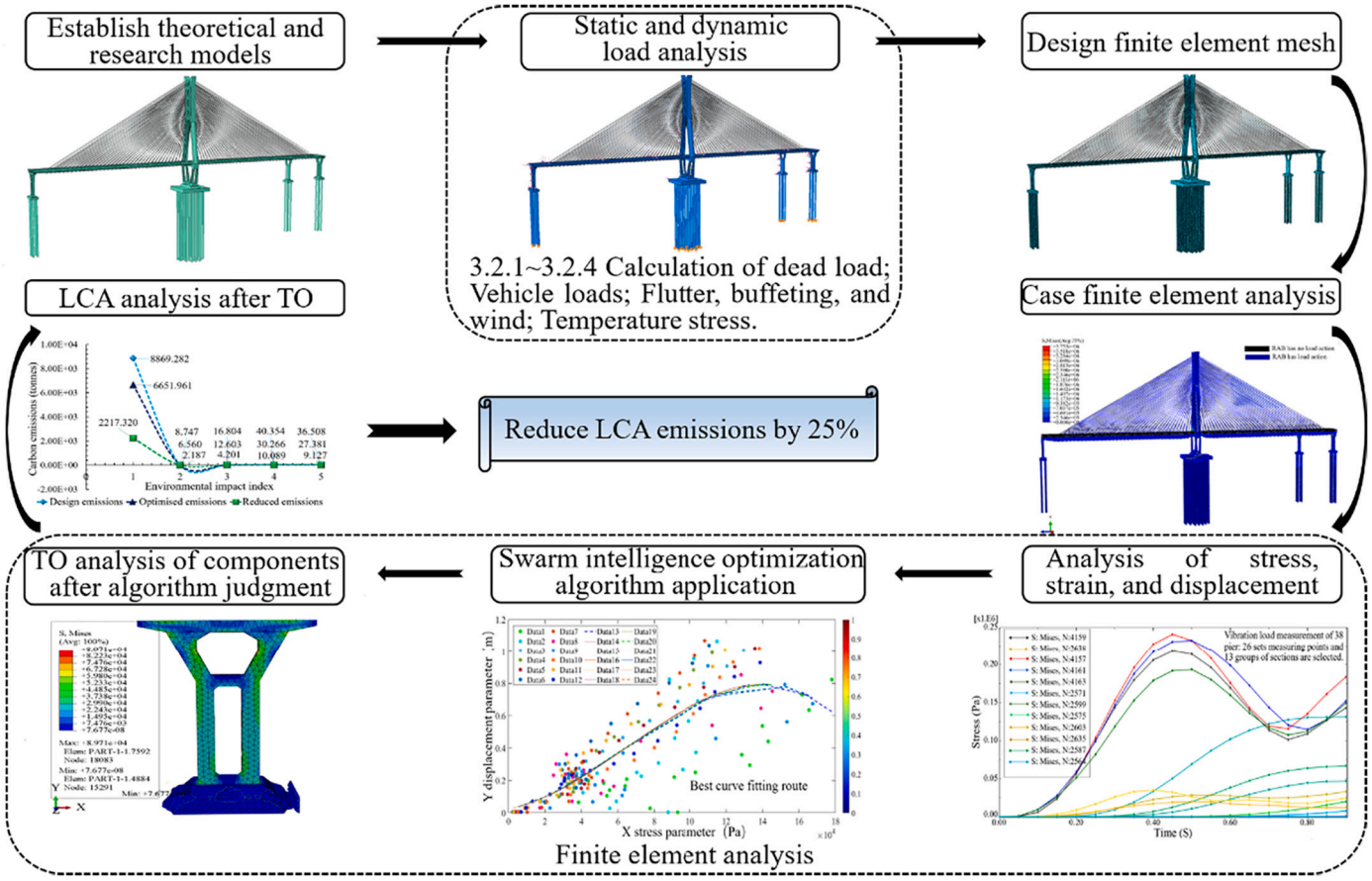

Fig. 1. Flow chart of TO for linear elastic structure.
Notes: The data in Fig has nothing to do with the research in this paper.

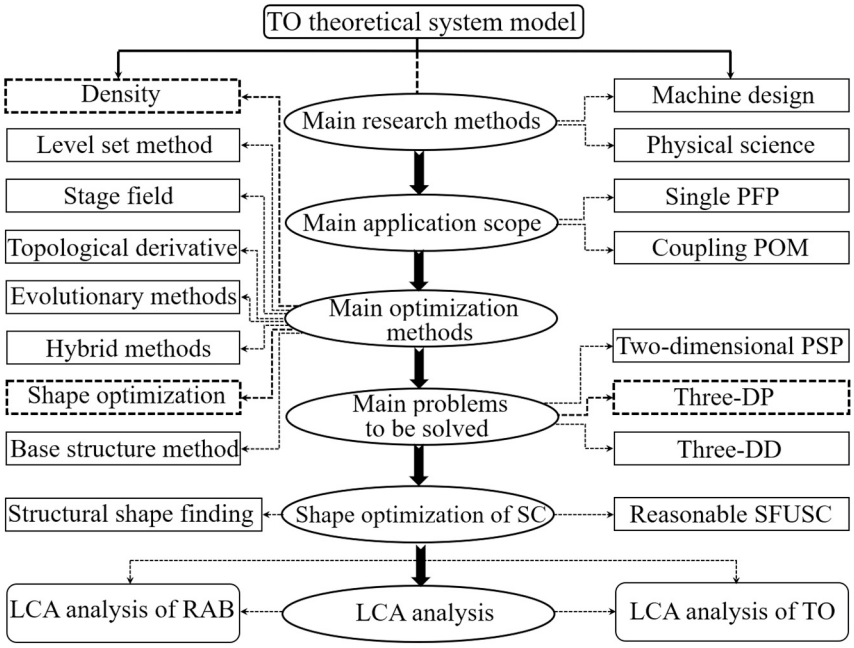

Fig. 2. Schematic diagram of TO theories and processes.
Notes: PSP = Plan stress problems; DD = Dimensional distribution; SFUSC = Structural form under specified conditions; SC = Structural components; PFP = physical field problem; POM = problem of MPF; DP = dimensional problem (this abbreviation only applies to Fig. 2).

and structural designers' redundant and conservative design of bridges needs further refinement and improvement, and there is still a particular gap with the green sustainable development design advocated. Moreover, this design concept also exists in other countries, especially developing countries.

The rest of this paper will be divided into the following sections: Section 2 methodology, four major categories of theoretical research systems related to the theme are established; Section 3 results, case research inference, and bridge TO process; Section 4 analysis, the components of the bridge were optimized for a second LCA data analysis; Section 5 conclusions, the paper's essential to research contents, limitations, and follow-up research directions are summarized.

2. Methodology

2.1. Research framework principle

Bendsøe and Kikuchi (Bendsøe and Kikuchi, 1988) proposed the TO principle in 1988 to optimise linear elastic structures. The researcher analyses anisotropic materials using a homogenization algorithm and establishes the finite element Eq. (1).

Kurian et al. (Kurian, 2021) studied the TO of Reinforced Concrete (RC) dapped-end beams under four conditions and established the minimum deflection optimization Eq. (2). Fig. 1 is the flow chart, research steps, and logical relationship of this research. Eq. (2) is suitable for the optimal arrangement of materials under given design spaces, loads, and boundary conditions. It is ideal for beams with simple structures in the given directions and magnitudes of action of external loads. The equation is generally used for structural optimization analysis carried out in laboratories.

Jewett and Carstensen (Jewett and Carstensen, 2019a) adopted the bilinear hybrid mesh TO algorithm framework. The element stiffness depends on the stress intensity, and the balance and convergence can be achieved by updating the stiffness matrix (). Eq. (3) is suitable for the studies of deep RC beams based on the strut-and-tie model.

Meng et al. (2020) applied the renewal equation of continuous, discrete variables to optimise the laminated materials, porous materials, and materials with a periodic composite structure and introduced the thermoelastic coupling Eq. (4) while considering the impact of temperature stress.

Zhang and Sun (Zhang and Sun, 2006) studied microscale optimization Eq. (5) for cellular materials and structure sizes. The structure was regarded as a homogeneous body and discretised as a finite element model. From Eqs. (2) and (5), we can find that they are established for the TO of a single member and that loads are generally imposed in the tests. However, many influencing parameters may be involved in the practical TO design of bridges (Torres-Machí et al., 2015; Cid Montoya et al., 2018). Thus, the research object in this paper is regarded as the statically indeterminate structural design.

Fig. 2 shows the whole process of TO in detail. Its purpose is to guide the modeling framework, thereby minimizing the structural weight and realising the environmental sustainability under design constraints (Zhou et al., 2020b).

Critical points for the design of cable-stayed bridges are determining the structural system, the sectional dimensions of members, calculation of the cable force distribution, the construction stage, and geometrically nonlinear effects. The structure is susceptible to bending failure, shear failure, and torsion failure under the action of external loads. The bearing loads mainly include dead loads, traffic and dynamic loads, permanent, variable and accidental loads, and seismic force (Wang et al., 2013). The following principles are adopted based on the complexity and uncertainty of this study:

(1) The structural TO of bridges at the design stage will not consider external loads in the construction process, and the focus is placed on the loads at the bridge's as-built stage.
(2) Taking papers involved in Table 1 and Fig. 2 as references. Only static and partially dynamic mechanical properties under environmental loads are studied (Mao et al., 2018). The structure must not be subject to body damage.
(3) The loads generated in TO are studied as dead loads (bridge structure gravity; additional gravity) and variable loads (vehicle

load; vehicle impact force; wind load and temperature influence), and accidental loads are not considered.

(4) This study proposes a new research method based on Table 1: Bidirectional TO of structures under multiple stresses (BTOS): i) Maximum principal stress of the structure. ii) Sensitivity vector. iii) Curve fitting approximation.

(5) In the environmental impact assessment of the bridge, the paper only the impact of raw materials at the design stage will be analysed.

(6) TO uses Abaqus CAE 6.14 for analysis; the sustainability LCA uses Open LCA1.10.3; the databases used include Ecoinvent, and Mat Web (Zhou et al., 2020a).

2.2. Theoretical framework of TO

According to Table 1 and the requirements of structural static stress, TO under external loads are: $\gamma_{i1}, \gamma_{i2}, \cdots, \gamma_{im}, \gamma_{l1}, \gamma_{l2}, \cdots, \gamma_{ln}$:

$$\sum_{i=1\cdots m}^{l=1\cdots n}\left(\gamma_{im,\cdots,km}^{ln,\cdots,kn}\right), min\ S=\sum_{\alpha=1}^{m}\omega_{i\alpha}\gamma_{i\alpha}+\sum_{\beta=1}^{n}\omega_{l\beta}\gamma_{l\beta}+\cdots\cdots+\sum_{i\cdots k}^{l\cdots k}\omega_{k(i\cdots k)(\alpha\cdots\beta)}\gamma_{k(l\cdots k)(\alpha\cdots\beta)} \tag{6}$$

$$\text{Meanwhile, } max\left[max\left(\sigma_{i\alpha\cdots l\beta\cdots k(\alpha\cdots\beta)}^{\text{Von Mises}}\right)^{k}\right]\le \underset{n\cdots m}{max}\left(\alpha^{i}\bigcap\alpha^{l}\cdots\cdots\bigcap\alpha^{n\cdots m}\right) \tag{7}$$

γ_{im} is the cell grid gravity under different loads (KN); γ_{ln} is the total gravity of the structure S (KN); $(\sigma_{i\alpha\cdots l\beta\cdots k(\alpha\cdots\beta)}^{\text{Von Mises}})^{k}$ are the Von Mises stress generated by the structure under the loads of Group K (kPa); $\alpha^{i}\bigcap\alpha^{l}\cdots\cdots\bigcap\alpha^{n\cdots m}$ are the maximum control Von Mises stress generated by the structure under the loads of Group K.

Eq. (8) expresses the TO process of the effective stress of a single load and combined loads and serves as the theoretical basis for studying the modeling framework.

If the effective unit retained under the loads is written as x_z, then:

$$\begin{cases} x_1\subset\{1,2,\cdots,m\} \\ x_2\subset\{1,2,\cdots,n\} \\ \vdots \\ x_z\subset\{1,2,\cdots,l,\cdots,k\} \end{cases} \tag{9}$$

Sensitivity vector: The displacement vector generated by each unit of the stress in the three-dimensional space $\{d\}^{k}$; the stress vector of the k^{th} unit is $\{\sigma\}^{k}=\{\sigma_{xx},\sigma_{yy},\sigma_{zz}\}_{k}^{l}$, which can be written as:

$$\{\sigma\}^{k}=[R]^{k}[G]^{k}\{d\}^{k} \tag{10}$$

where $[R]^{k}$ is the elasticity modulus matrix; $[G]^{k}$ is the geometry modulus matrix.

The sensitivity variation of the displacement vector generated during the optimization is $\{\triangle\sigma\}_{k}^{v}\begin{bmatrix}\triangle\sigma_x\\ \triangle\sigma_y\\ \triangle\sigma_z\end{bmatrix}_{k}^{v}=[R]^{k}[G]^{k}\{\triangle d\}^{k}$. Substitute Eq. (9) into it to obtain:

$$\begin{bmatrix}x_1\\ x_2\\ \vdots\\ x_z\end{bmatrix}\{\sigma\}^{k}=\begin{bmatrix}\sum_j x_{1j}\left(u^{ij}\right)^{T}\\ \sum_j x_{2j}\left(u^{ij}\right)^{T}\\ \vdots\\ \sum_j x_{zj}\left(u^{ij}\right)^{T}\end{bmatrix}\left[K^{i}\right]\left\{d^{i}\right\} \tag{11}$$

$x_1,\cdots,x_z$ are the number of lines of the matrix $[R]^{k}$; $[G]^{k}$; $\{\sigma\}^{k}$ are the displacement sensitivity vector of k units; $x_{1j}\left(u^{ij}\right)^{T}(j=1,2,\cdots,n)$ are that

$$\begin{cases} \gamma_{i\alpha}\in\{0,1\},\alpha=1,2,\cdots,m & \text{The } i-\text{load retains the effective element after } \alpha \text{ iteration} \\ \gamma_{l\beta}\in\{0,1\},\beta=1,2,\cdots,n & \text{The } l-\text{load retains the effective element after } \beta \text{ iteration} \\ \gamma_{k(l\cdots k)(\alpha\cdots\beta)}\in\{0,1\},\ \alpha\cdots\beta=1,\cdots,k & \text{Effective iteration under other loads} \end{cases} \tag{8}$$

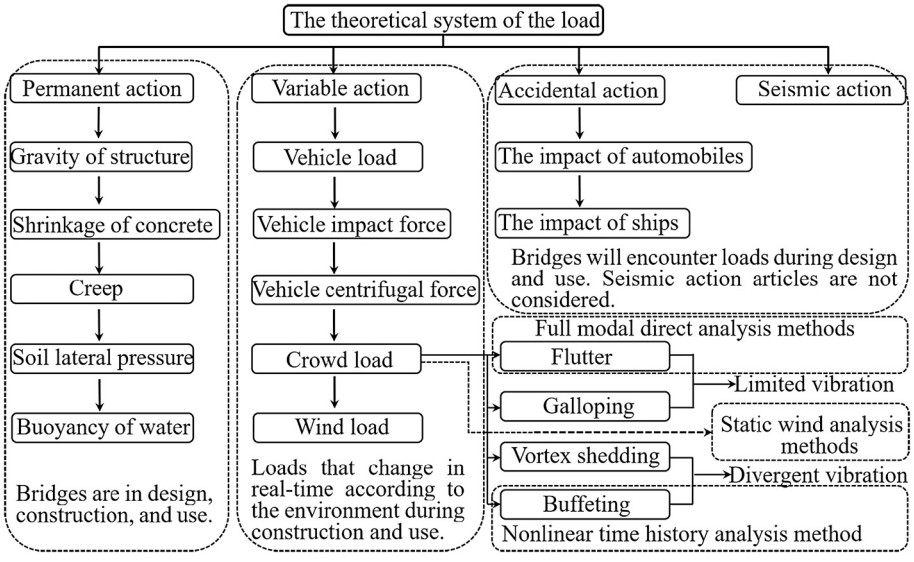

Fig. 3. The combined effect model system of bridge design loads.

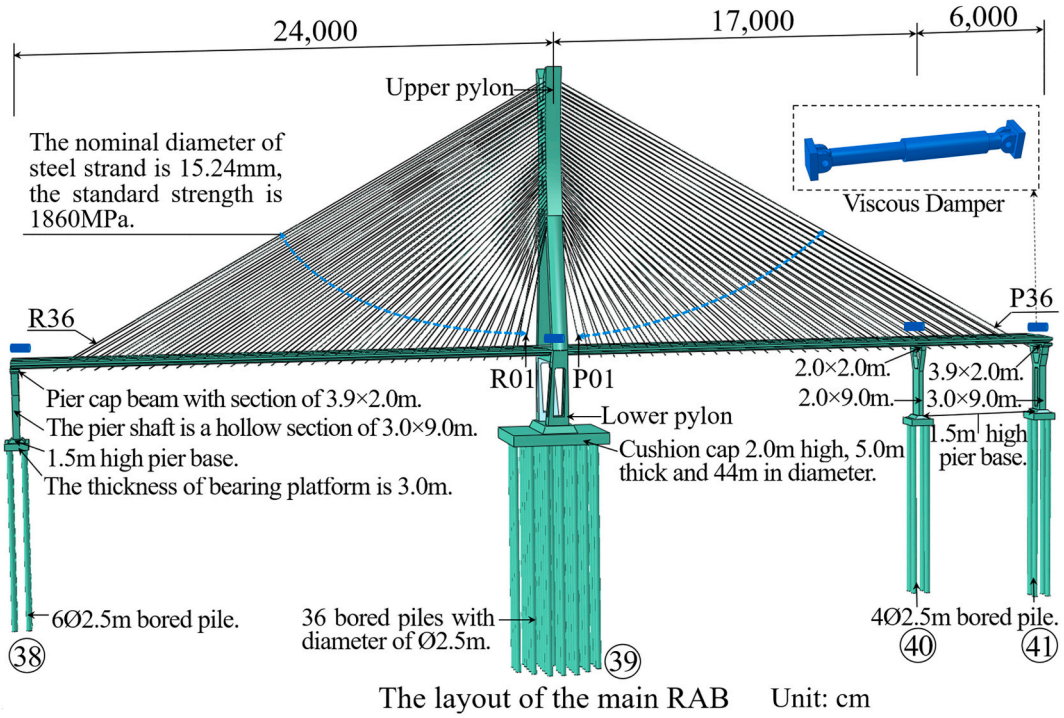

Fig. 4. Layout of main bridge of cable-stayed bridge.

the j^{th}unit causes the displacement of i units; $x_{zj}(Z = 1,2,3,\cdots,n;j = 1,2,3,\cdots,n) \times (u^{ij})^T(j = 1,2,3,\cdots,n)$ are the equilibrium equation of loads. The stress variation of the k^{th} unit can be expressed as $\begin{bmatrix} \triangle\sigma_x \\ \triangle\sigma_y \\ \triangle\sigma_z \end{bmatrix}_k^v = \begin{bmatrix} \widetilde{u}_{ik}^1 \widetilde{u}_{ik}^2 \widetilde{u}_{ik}^3 \end{bmatrix} \left[k^i\right]\left\{d^i\right\}$. Thus, the Von Mises stress of the k^{th} unit is written as $\widetilde{\sigma}_k^{vm} = \sqrt{\sigma^{1\,2}_x + \sigma^{1\,2}_y - \sigma^x\sigma^y + 3Y^{12}_{xy}}$, and the sensitivity vector of the k^{th} unit can be written as

$$\triangle\sigma_k^{vm} = \widetilde{\sigma}_k^{vm}\sigma_k^{vm} \tag{12}$$

In the process of structural TO, each part of the bridge structure is subject to the Mises stress analysis to determine whether it is a valid or invalid member. Subsequently, TO is directly conducted to eliminate weak members and reduce materials consumption. Finally, the sensitivity vector is used to determine the rationality of the TO.

Table 2
Statistical data of main bridge materials.

Component name	Asphalt concrete (t)	Concrete (100 t)	Steel strand (t)	Other steels (t)
Pier 39	0.00	665.50	0.00	1405.82
Piers 38, 40, 41	0.00	213.33	0.00	611.21
Main tower	0.00	219.37	166.98	1508.80
Anti-collision pier	0.00	564.36	0.00	1936.82
Main beam	2982.15	276.66	244.53	2049.80
Transverse beam	0.00	51.51	189.47	326.10
Stay cable	0.00	0.00	0.00	111.82

$$\sum_{i=R}^{i=E} E_m = \begin{cases} R_m = \sum_i^j \left[\left(M_{qi} \times \lambda_i + \cdots + M_{qj} \times \lambda_j\right) \times \lambda_\mu\right] \quad (19) M_m = \sum_i^j \left\{\left[G_{im} \times (1+\alpha) \times T_{im} \times \left(\lambda_\mu \oplus \lambda_\nu\right)\right] + \cdots + \left[G_{jm} \times (1+\alpha)\right.\right. \\ \left.\left. \times T_{jm} \times \left(\lambda_\mu \oplus \lambda_\nu\right)\right]\right\} \quad (20) \; P_m = W_m \times \lambda_p \times T_p \quad (21) E_m = \sum_{\text{Start}}^{\text{End}} (R_m + M_m + P_m) \quad (22) \end{cases}$$

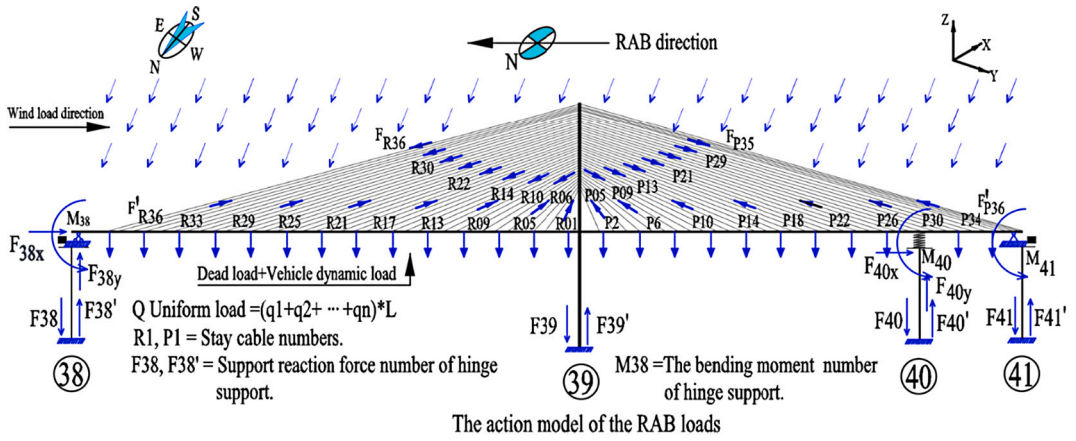

Fig. 5. Constraint diagram of RAB load.

Table 3
TO unit partition.

Part name	Unit division	Number	Unit name	Material
Pile foundation, C35	38; 39; 40; 41	4 pieces	PF 38; 39; 40; 41	RC
Pile platform; Pier base, C40	38; 39; 40; 41	4 pieces	PP 38; 39; 40; 41	RC
Pier column, C40	38; 41	2 pieces	PC 38; 41	RC
Pier column; Bearing pad stone, C50	40	1 piece	PB 40	RC
Bent cap, Bearing pad stone, C50	38; 41	2 pieces	BB 38; 41	RC
Girder, C55	38–39	1 piece	G 38–39	RC
	39–41	1 piece	G 39–41	RC
Pylon, C50	39–1	1 piece	P 39–1	RC
	39–2	1 piece	P 39–2	RC
	39–3	1 piece	P 39–3	RC
Stay cable	39 ~ R	1 piece	S 39 ~ R	Steel strand
	39 ~ P	1 piece	S 39 ~ P	Steel strand

Notes: Concrete = C (this abbreviation only applies to Table 3).

2.3. Swarm intelligence optimization algorithm curve fitting approximation

Because of the discrete data after 2.2 TO, the accuracy and scientific of the data can be improved by using the scientific higher mathematics calculation method based on sensitivity analysis and the swarm intelligence optimization of the curve fitting approximation calculation method is introduced (Kobayashi et al., 2020).

Basic principle: data analysis, the function value of the approximation function at the sampling point is determined, and the curve fitting approximation method is adopted. Like data interpolation, the curve fitting function approximation method.

$$\begin{matrix} x & x_1 & x_2 & x_3 & \cdots & x_k & \cdots & x_n \\ y & y_1 & y_2 & y_3 & \cdots & y_k & \cdots & y_n \end{matrix} \longrightarrow y = f(x) \longleftarrow y = g(x)$$

The constructor $g(x)$ approximates the unknown function $f(x)$, Make error Delta $\delta_i = g(x_i) - f(x_i)$ $(i = 1, 2, 3, \cdots, n)$ is the minimum. The least-square method (also known as the least square method) is a mathematical optimization technique that seeks the best function matching of data by minimizing the sum of squares of errors.

Let $p(x)$ be a polynomial function and $p(x) = a_m x^m + a_{m-1}x^{m-1} + \cdots + a_1 x + a_0$, is the smallest, then $\sum_{i=1}^{n} [p(x_i) - y_i]^2$ is the approximation function of the original function $y = f(x)$.

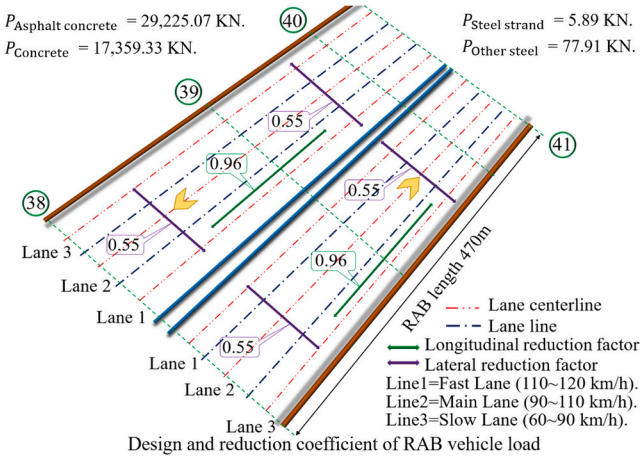

Fig. 6. Design and reduction coefficient model of RAB vehicle load.

The method of curve fitting is as follows:

Polyfit (…) language is used in MATLAB to determine the polynomial fitting function. Function performance: get the least square fitting polynomial coefficient.

Call format: (1)> > $x = [x_1, x_2, \cdots, x_n]$; (2) $y = [y_1, y_2, \cdots, y_n]$; (3) p = polyfit(x, y, m); (4) $[p, s]$ = polyfit(x, y, m); (5) $[p, s, m]$ = polyfie(x, y, m).

According to the sample data x and y, a polynomial P of degree m and the point error data s are generated. Mu is a binary vector, Mu (1) is mean (x), and Mu (2) is STD (x).

2.4. The theoretical system of the load

Long-span cable-stayed bridges adopt deterministic methods in the design and construction stages. For example, 'Technical Standards,' 'General Specification for Design,' 'Code for Design of Bridges with Wind Resistance,' etc., do not reveal the variation of structural material parameters, geometry, and external load's Intrinsic impact on bridges. As a high-order hypostatically indeterminate flexible structure, the structural response of long-span cable-stayed bridges is particularly complex (Hu et al., 2019; Zhou et al., 2022).

The American AASHTO code, the British BS5400 code, the Canadian CAN-CSA-S6–00 code, and the European Eurocode code is the same as the classification of the design load of bridges, mainly divided into permanent action, variable action, accidental action, and seismic action. Among them, the wind load of the variable gear is the focus of bridge structure research (Shao et al., 2018). The wind-induced vibration of

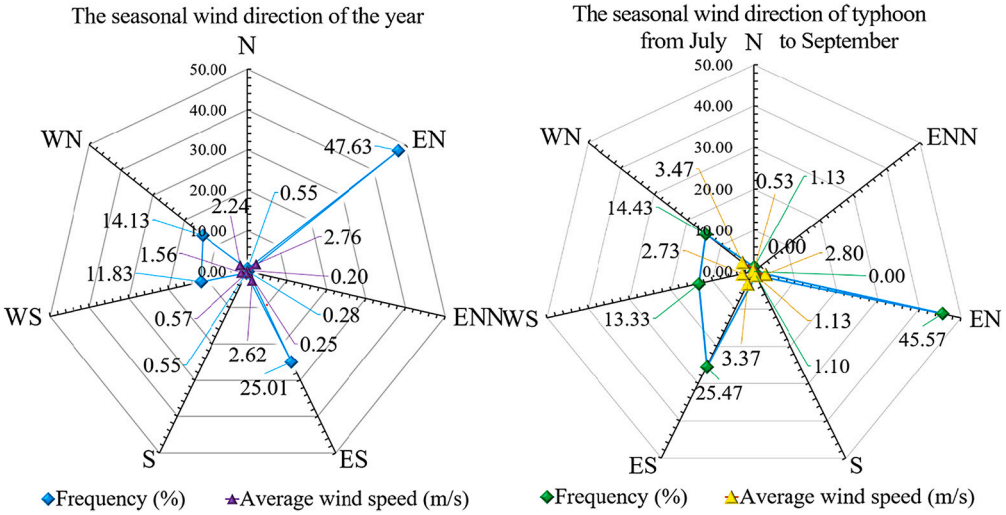

Fig. 7. Wind rose diagram of year and typhoon season (Cid Montoya et al., 2021). (For interpretation of the references to colour in this figure legend, the reader is referred to the web version of this article.)

bridge structures is divided into two categories: the aerodynamic instability divergent vibration caused by the destructive consequences of the bridge caused by the wind power, such as flutter and galloping vibration; the component fatigue and driving caused by the wind power. Safely limited vibration. Such as vortex-induced vibration and buffeting (Cid Montoya et al., 2021).

The critical factors for the occurrence of a flutter: one is the aerodynamic factors, mainly the aerodynamic shape of the structural section; the other is the structural factors, which are primarily the stiffness, damping, and quality of the structure (Fig. 3).

The buffeting is mainly the forced vibration caused by the pulsating wind component in the incoming atmospheric flow on the structure, mainly including the wake buffeting caused by the wake of the system itself, the path of the adjacent upstream structures, and the atmospheric turbulence. Among them, the pulsating wind in the atmosphere plays an important role and is also part of the analysis of this paper.

The flutter analysis of bridge structure is a systematic project involving all contents of wind tunnel test research, wind resistance analysis, and aerodynamic technology. This paper focuses on the LCA and TO study, and the analysis method of the bridge's wind resistance system is performed according to the model in Fig. 3 (Wang et al., 2014).

2.4.1. Model of flutter force

Main girder (separation-flow torsional flutter theory of bridge structures, and Sarkar's aerodynamic model only analyzes the main beam (Sarkar et al., 1994):

$$L_{se} = \frac{1}{2}\rho U^2(2B)\left(K^2H_4\frac{h}{B} + K^2H_6\frac{p}{B} + K^2H_3\alpha + KH_1\frac{h}{U} + KH_5\frac{P}{U} + KH_2\frac{B\alpha}{U}\right) \tag{13}$$

$$D_{se} = \frac{1}{2}\rho U^2(2B)\left(K^2P_6\frac{h}{B} + K^2P_4\frac{p}{B} + K^2P_3\alpha + KP_5\frac{h}{U} + KP_1\frac{P}{U} + KP_2\frac{B\alpha}{U}\right) \tag{14}$$

$$M_{se} = \frac{1}{2}\rho U^2(2B^2)\left(K^2A_4\frac{h}{B} + K^2A_6\frac{p}{B} + K^2A_3\alpha + KA_1\frac{h}{U} + KA_5\frac{P}{U} + KA_2\frac{B\alpha}{U}\right) \tag{15}$$

H_k is aerodynamic derivative; α is the instantaneous angle of attack of the main beam; $\rho = 1.225$ kg/m^2 is air density; U is wind speed; K is reduced frequency; H_i, P_i, A_i are 18 flutter derivatives; vertical h, lateral p, the displacement and velocity in three directions of torsion α; L_{se}, D_{se}, M_{se} are the horizontal and vertical lift, resistance, and lift moment

Table 4
Related performance parameters of RAB structural materials (OBrien et al., 2020).

AS	Concrete grade	AT	CS	Elastic modulus	Poisson's ratio
Pile foundation	C35	5 °C	23.290	3.133	0.243
		10 °C	23.483	3.141	0.244
		20 °C	23.702	3.150	0.244
		30 °C	23.483	3.141	0.244
Pier base, Pier column	C40	5 °C	25.865	3.233	0.249
		10 °C	26.088	3.241	0.249
		20 °C	26.342	3.250	0.250
		30 °C	26.088	3.241	0.249
Pylon	C50	5 °C	28.383	3.318	0.254
		10 °C	30.593	3.384	0.258
		20 °C	33.068	3.450	0.263
		30 °C	30.593	3.384	0.258
Girder	C55	5 °C	31.645	3.413	0.260
		10 °C	34.295	3.480	0.266
		20 °C	37.445	3.550	0.272
		30 °C	34.337	3.481	0.266
Stay cable	ASTM A416-90a 270 grade	5 °C	Standard strength1,860 MPa	1.95×10^5 MPa	Control stress 1395 MPa
		10 °C			
		20 °C			
		30 °C			

Notes: AS = Application site; AT = Ambient temperature; CS = Compressive strength.

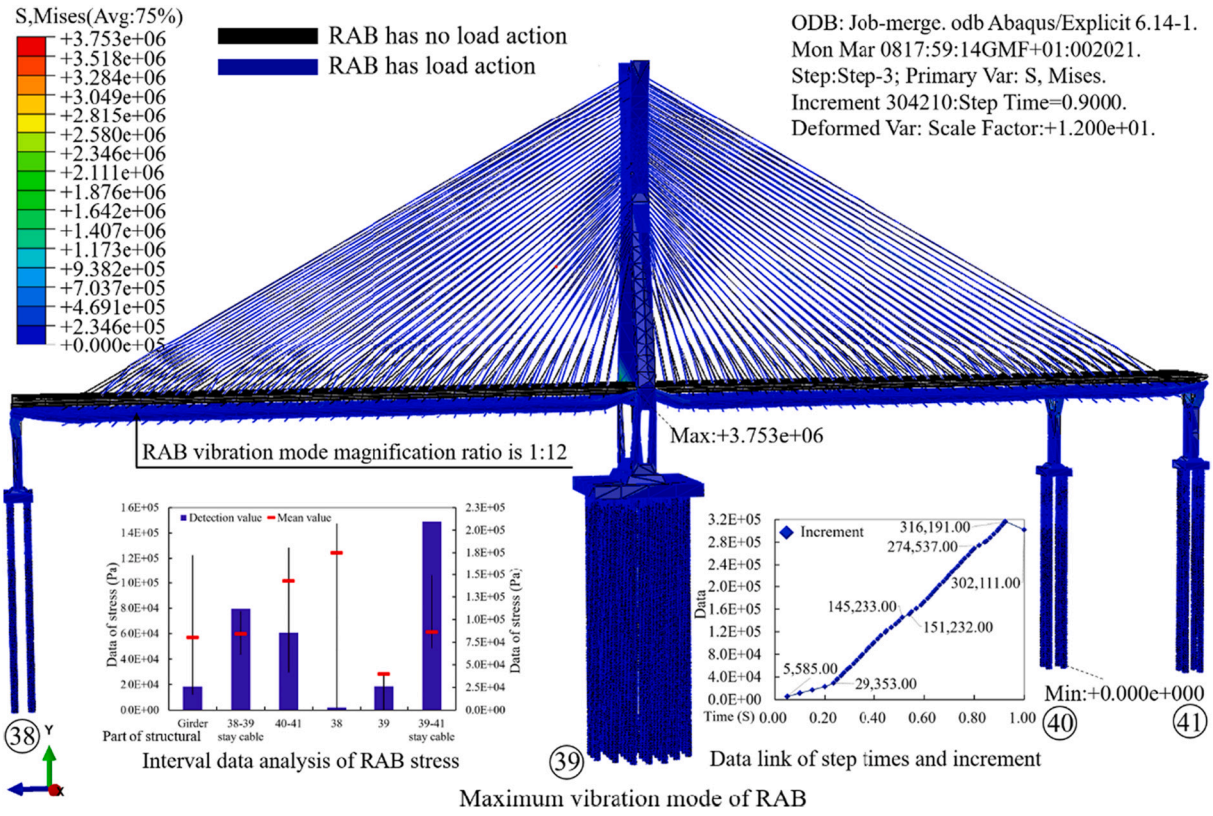

Fig. 8. Vibration mode of RAB under combined load (maximum elements).

aerodynamic force on flutter force.

According to China's 'Code for Design of Highway Bridges Against Wind,' the critical flutter wind speed is calculated and stipulated that the necessary flutter wind speeds are 111.8 m/s, 97.3 m/s, 120.9 m/s when the initial wind attack angles are 0, +3, and − 3 (according to Eqs. (19–21), the relevant wind tunnel test data test is required, and this study does not have the appropriate conditions) (Zhang et al., 2016).

2.4.2. Model of buffeting force

The buffeting force is caused by the pulsating wind and is calculated using Scanlan's quasi-steady aerodynamic equation and corrected using Davenport's (Davenport, 1962) aerodynamic admittance function, and can be expressed as:

$$L_b(t) = \frac{1}{2}\rho U^2 B\left[2C_L\chi_{Lu}\frac{u(t)}{U} + \left(C_L' + C_D\right)\chi_{Lw}\frac{W(t)}{U}\right] \tag{16}$$

$$D_b(t) = \frac{1}{2}\rho U^2 B\left[2C_D\chi_{Du}\frac{u(t)}{U} + \left(C_D' - C_L\right)\chi_{Dw}\frac{W(t)}{U}\right] \tag{17}$$

$$M_b(t) = \frac{1}{2}\rho U^2 B^2\left[2C_M\chi_{Mu}\frac{u(t)}{U} + C_M'\chi_{Mw}\frac{W(t)}{U}\right] \tag{18}$$

χ_{Lu}, χ_{Du}, χ_{Mu}, χ_{Lw}, χ_{Dw}, χ_{Mw} are the aerodynamic transfer function; C_L, C_D, C_M are the three-component force coefficients of the wind axis; C_L', C_D', C_M' are the corresponding derivatives of the three-component force of the wind axis; u, w are the pulsating wind speed (m/s).

2.5. Sustainable environmental impact modeling

The sustainability assessment framework for bridges covers related technical, economic, environmental, and social issues. We have mentioned that only the sustainable ecological impact at the design stage is studied (Goverse et al., 2001). Zhou et al. (2020b)) created a practical assessment framework and theoretical model for the three pillar issues (environmental, economic, and social impacts) of bridges.

2.5.1. Framework and parameters

International Organization for Standardization (ISO) stipulates the LCA standard research framework: Goal and scope definition, inventory analysis, impact assessment, and interpretation. The main parameters of the study are Acidification Potential (AP); Particulate Matter Formation Potential (PMFP); Global Warming Potential (GWP); Free Water Eutrophication Potential (FEP); Smoke, Dust, and Wasted Potential (WP). LCA is divided into five stages: Survey and design, Material manufacturing, Construction and installation, Maintenance and operation, and Disassembly and recycling (Zhou et al., 2020b).

2.5.2. Research external conditions

The European Commission Joint Research Centre uses the midpoint and endpoint models. Yang et al. (Yang et al., 2018) use building information modeling to model site construction.

Considering the above representative research results and TO conclusions, the midpoint and the endpoint used to build an LCA model and to choose sufficient raw data and practical evaluation, the focus is the environmental impact at the design stage.

2.5.3. Impact factor

Zhou et al. (Zhou et al., 2020a) studied the influencing factor values of each stage of the cable-stayed bridge LCA, which laid the foundation for this paper. Open LCA1.10 software analysis needs to set the impact factor of each stage (range from 1.00 to 1.50). In this study, the impact factor of the material design stage is 1.06.

2.5.4. Modeling framework

The environmental impact is:

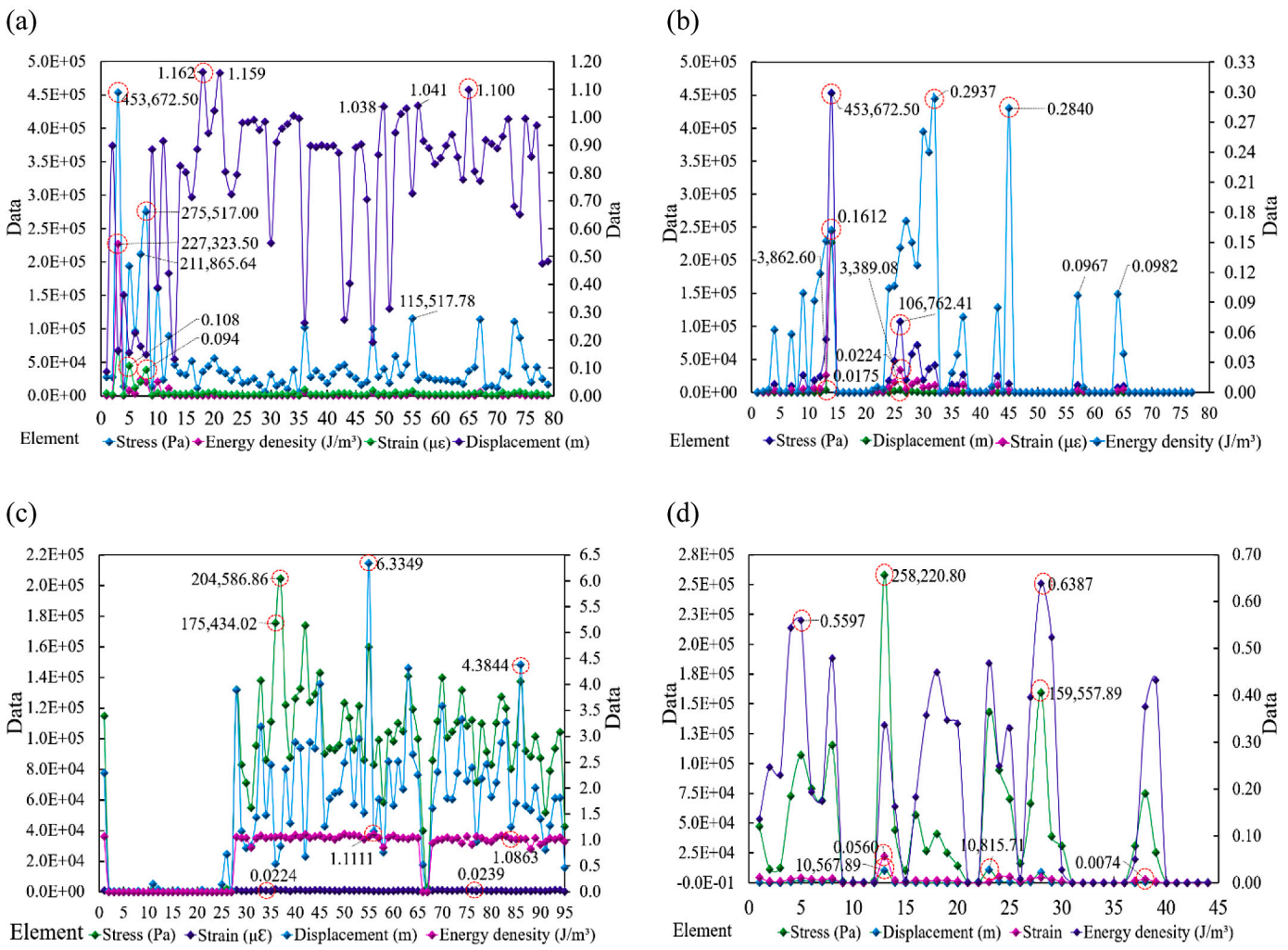

Fig. 9. Component Finite Element Data Analysis of RAB. (a) Main beam. (b) Main tower. (c) Stay cable. (d) 38#, 40# and 41#..

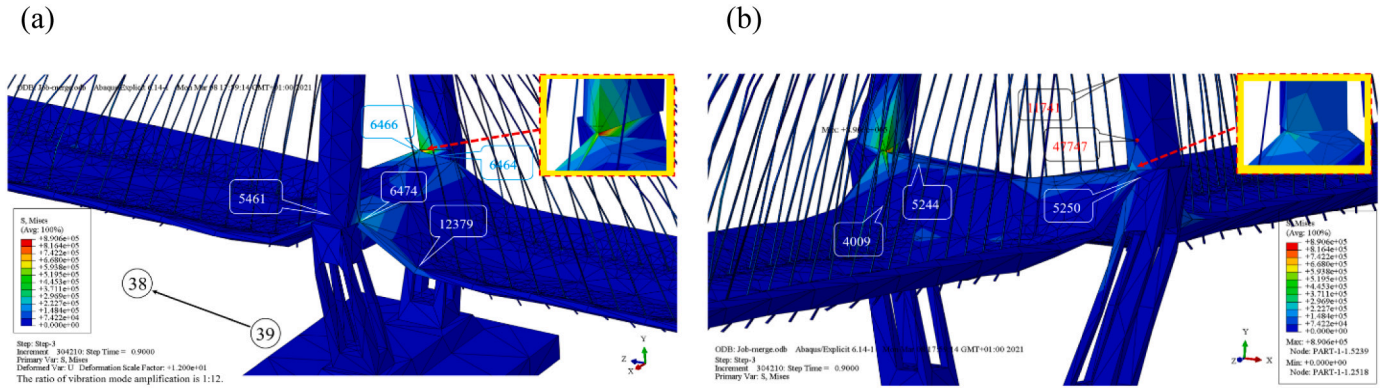

Fig. 10. Special elements analysis. (a) Distribution of maximum stress elements on bridge deck. (b) Distribution of maximum stress elements on bridge pylon (4009, 5244 is under deck).

where R_m, M_m, $P_m$are the environmental pollution of raw materials (kg); the environmental pollution of the equipment (kg); the environmental pollution of the staff (kg); M_{qi}, M_{qj} is the quantity of the material *i* and j (kg); G_{im}, G_{jm} is the fuel consumption and power consumption of equipment *i*, *j* (kg/h, kWh); W_m is the total number of staff (Persons); λ_i, λ_j is the physical and chemical environmental emission coefficient of the material i and j (kg); λ_μ is the impact factor of the material,μ; λ_μ, λ_ν is the physical and chemical environmental emission coefficient of the oil-bearing material, μ and ν (kg/kg); λ_p is the environmental impact factor of staff (kg/working day/person); T_{im} is the normal working hours of equipment (h); $\oplus$is logic 'Or'; T_p is total working hours of staff (working day); E_m is the total quantity of environmental pollution generated at the

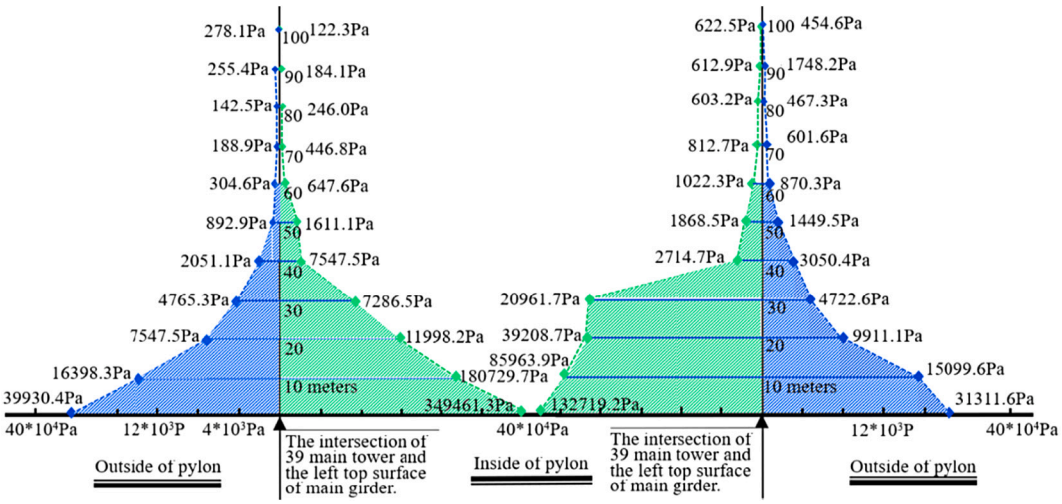

Fig. 11. Main tower 39 stress gradient.

Table 5
Summary of the stress indexes of six parts of RAB.

Groups	1	2	3	4	5	6
Girder	18,250.79	81,834.54	17,072.38	24,005.77	79,081.15	134,449.21
38–39 stay cable	79,669.71	109,322.34	101,586.21	79,286.84	88,286.05	78,780.07
40–41 Pier	60,861.76	66,173.36	180,756.64	154,364.06	41,775.87	58,918.99
38 Pier	2029.82	94,259.65	25,452.25	5633.69	39,264.78	28,062.85
39 Pier	18,691.48	15,096.44	26,583.56	39,335.48	42.54	7821.16
39-41Stay cable	148,919.83	115,413.73	81,171.76	72,937.16	81,983.13	68,374.01
Groups	7	8	9	10	11	12
Girder	172,291.49	34,652.20	37,391.11	41,832.82	43,558.46	80,168.70
38–39 stay cable	67,451.76	73,512.78	84,955.92	86,473.27	61,203.39	83,944.11
40–41 Pier	48,734.84	76,239.13	211,039.90	211,039.90	155,813.14	142,614.76
38 Pier	29,107.78	17,703.89	207,114.97	187,416.27	205,269.15	174,698.29
39 Pier	10,011.83	24,090.70	39,208.68	0.00	0.00	39,844.66
39-41Stay cable	75,508.47	87,231.28	103,889.62	96,963.19	71,533.10	86,192.13

design stage (kg).

3. Results

Guo et al. (2020) studied the dynamic response of long-span double-tower cable-stayed bridges under the impact of a ship and the mechanical properties of and damage to bridges caused by local scour, indicating that the studies of solid effect modeling are assumed to be more scientific. Jewett and Carstensen (2019b)) surveyed the reinforcement design of an RC structure after TO and gave an optimization design for local members. Bao tong Li et al. (Li et al., 2017) proposed achieving the optimal layout of a welded box girder structure using the structural foundation method to reduce carbon dioxide emissions. The authors searched Scopus for studies on TO and the environmental sustainability of bridges. We concluded that no complete studies were being found about TO on the ecological sustainability of 3D solid bridges.

3.1. Case description

The study case is the Rui An Bridge (RAB), a Grade one highway bridge located in Rui An City, Zhe Jiang Province, China. The RAB is composed of the main bridge (470 m) and the approach bridge (2486 m), with a total length of 2956 m (Guide, 2017).

The main span deck has six lanes in two directions, with the designed speed limit of 100 km/h. The span arrangement of (240 + 170 + 60 m) was adopted. Specifically, the main span is 240 m long and 33 m wide. The main beam has an overall width of 36.8 m and a central sectional central height of 3.2 m. The top plate of the box girder is 0.28 m thick, and the bottom plate is 0.4 m wide; the lower angle web is 0.25 m thick, and the web is 0.4 m thick (the research object of this study is the main bridge).

Fig. 4 shows the structural the RAB main bridge's composition and profile diagram and shows the materials of the main bridge. The optimal combination of structural dimensions is studied under the designed load constraints. An analysis is conducted when external loads such as temperature stress and wind force are increased (Feng et al., 2020). The materials consumption after the TO is obtained, and then the LCA software is used to realize the sustainability of the bridge's environmental impact (Zhou et al., 2020b)

The major materials consumption of the RAB, as shown in Table 2, is calculated based on the design drawings. The main distribution of RC: Pier 39 weighs 66,550 t, consisting of C35, C40, and C50 concretes. The anti-collision pier was built from bituminous concrete, weighing 56,436 t; the main beam was built from C55 high-performance concrete, weighing 27,666 t. Reinforcement distribution: main beam Φ20; Φ16; Φ12; transverse beam Φ12. Other steel products include stay cables (1398.28 t) and steel wires (1301.16 t).

The RAB's concretes are mainly distributed in Pier 39 (38,274 m^3), the anti-collision pier (24,592 m^3), the primary and transverse beams (14,072.3 m^3), and Piers 38, 40, and 41 (9398 m^3). Class I and II reinforcements are mainly distributed at the main beams and central tower, accounting for 72.22% of the total reinforcements.

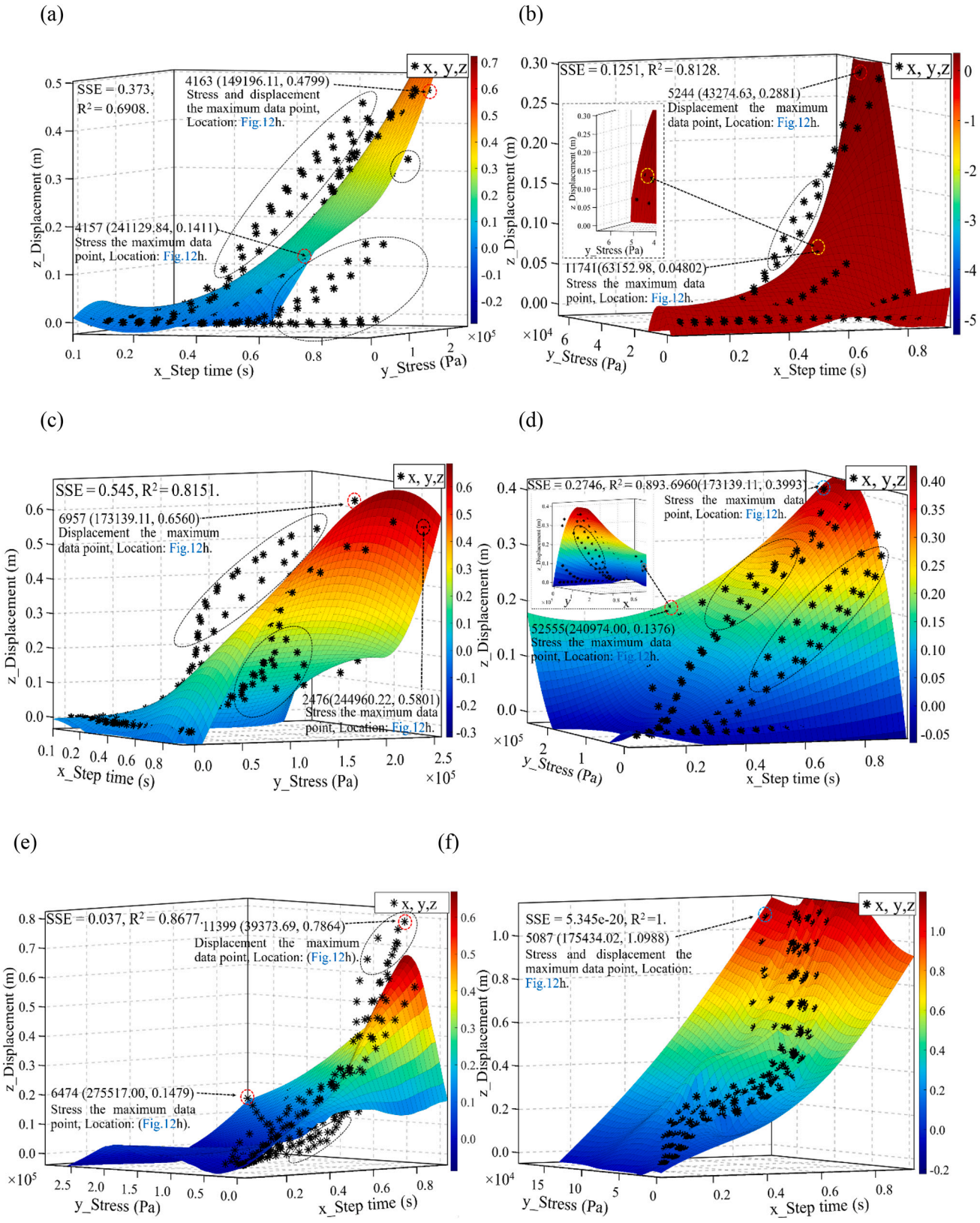

Fig. 12. Analysis of RAB. (a) 38 pier polynomial fit. (b) 39 pier Polynomial fit. (c) 40 pier polynomial fit. (d) 41 pier Polynomial fit. (e) Girder Locally weighted smoothing linear regression fit. (f) 38–39 stay cable thin-plate spline interpolant fit. (g) 39–41 stay cable Linear model Polynomial fit. (h) The maximum displacement and stress distribution of each part of the bridge.

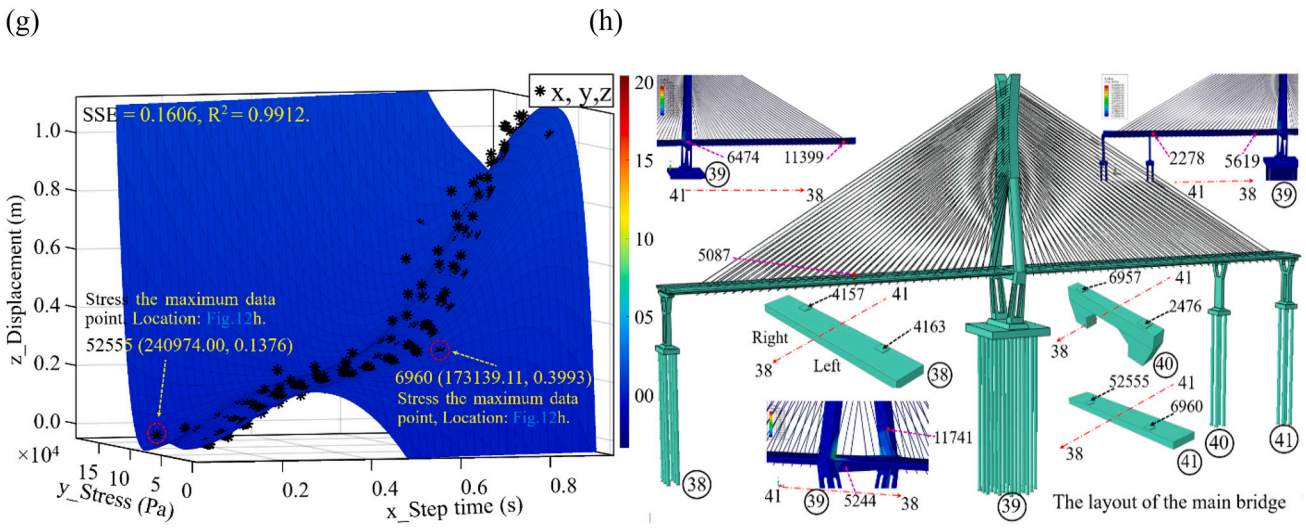

Fig. 12. (*continued*).

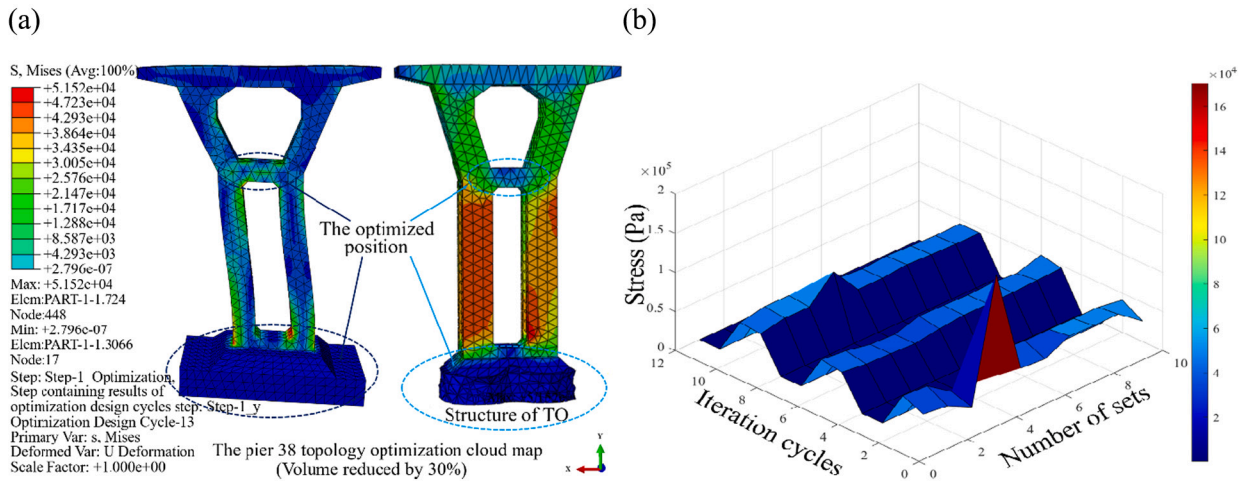

Fig. 13. Analysis of 38#. (a) Comparison of topological optimization cloud maps of Pier 38 (70% of the original volume). (b) Changes in various indicators during the Pier 38 iteration cycle.

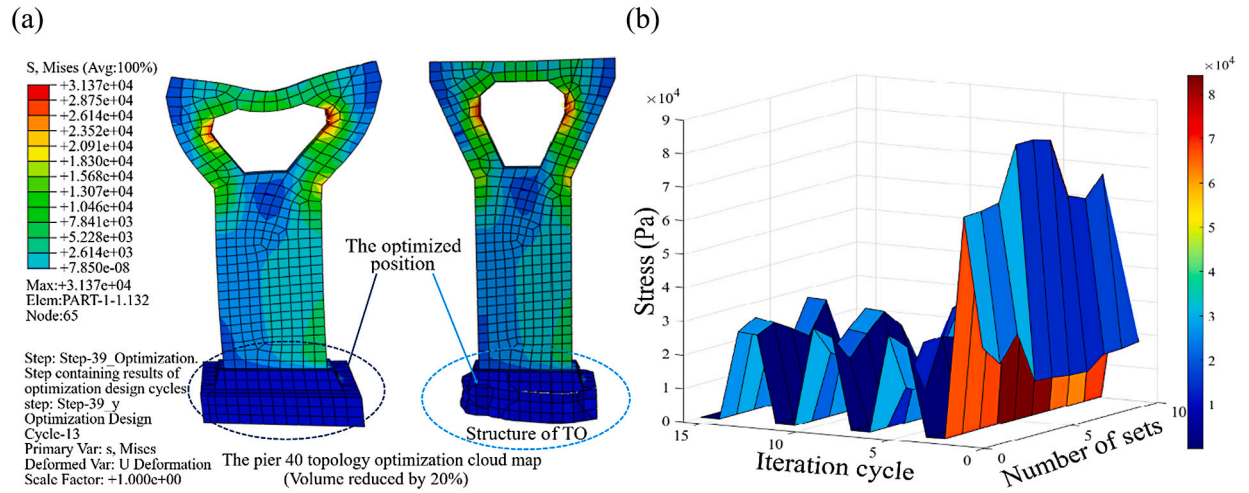

Fig. 14. Analysis of 40#. (a) Comparison of topological optimization cloud maps of Pier 40 (80% of the original volume). (b) Changes in various indicators during the Pier 40 iteration cycle.

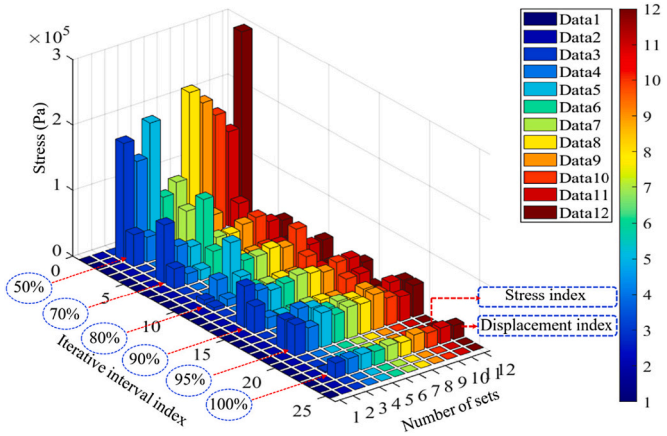

Fig. 15. Changes in various indicators during the Pier 40 iteration cycle.

Table 6
TO research progress data (the calculation method is the same as Section 3.3.2).

Bridge part	Volume ratio	NI (cycle)	Stress(Pa)	Sensitivity	Displacement(m)	Conclusion
38	0.50	23	51,800	2,381,400–3,199,800	0.479	Failed
	0.70	13	51,521.4	683,470–761,780	0.479	Succeeded
	0.80	13	51,714.7	104,500–110,650	0.482	Failed
40	0.60	25	32,670	11,340,000–27,308,000	17.137	Failed
	0.70	15	31,360	77,546–86,483	0.915	Failed
	0.80	13	31,370	38,147–41,045	0.518	Succeeded
	0.90	11	31,370	40,872–41,945	0.318	Failed
41	0.50	25	67,200	4,407,800–2,275,000	9.773	Failed
	0.70	17	54,550	4,407,800–2,275,001	4.086	Failed
	0.80	13	54,270	40,170–232,590	2.584	Failed
	0.90	13	54,271	129,970–347,330	1.551	Failed
	0.95	11	54,270	561,010–653,880	1.401	Failed
	1.00	0	54,270	1540–154,250	1.075	Failed

Notes: NI = Number of iterations (cycle); Volume ratio = (original volume - reduced volume)/original volume = Remaining volume ratio.

3.2. Calculation of RAB load

The schematic diagram of the RAB loads is analysed and plotted, as shown in Fig. 5, based on the design documents and the referenced articles. The figure indicates the force sizes of the loads and applied forces by purple lines.

The changes or uncertainties of the load impact factors will significantly influence TO. Based on reliability and robustness, the TO is the primary paradigm used to solve tensions (Wang and Gao, 2019). The analysis in this study is carried out based on the design documents, and the changes in boundary conditions are specific. The following two combinations of loads are mainly considered for the RAB:

(1) Dead load + Vehicle load (Vehicle - over grade 20; Trailer - grade 120).
(2) Dead load + Vehicle load + Wind load + Temperature variation (the research group discussed and decided to select the maximum load combination for analysis).

The RAB extends from northeast to southeast. Pier 38 is located on the northeast side, and pier 41 is located on the southwest side. Pier 38 was designed with movable hinged support, and pier 40 was designed with an auxiliary pier and portable hinged support. Pier 41 was designed with fixed, hinged support. Fig. 5 is a schematic diagram of the directions in which the RAB loads act and relevant analysis. The loads mainly include the bridge structure gravity; vehicle load; vehicle impact force; wind load; and temperature stress.

Table 3 shows the unit optimization analysis after the RAB is divided into 20 parts according to the structural composition.

3.2.1. Dead load

Dead load = Structure gravity = Material volume -Weight (dead load range: calculation of the weight of bridge's main members), as shown in Table 2 and Fig. 6.

3.2.2. Vehicle loads

By reference to JTG D60–2015 General Specifications for Design of Highway Bridges and Culverts (CC Highway, 2015) on the value of vehicle load, the value standard of automobile load is selected according to the standard value of uniform load is q_k = 10.5KN/m; the concentrated load is p_k = 360 KN. $P_{\text{Vehicle load}} = l_{\text{Number}} \times (L_{\text{Long}} \times q_k + p_k)$ = 31,770 KN.

As shown in Fig. 6, the transverse reduction coefficient of the RAB's vehicle load is 0.55, and the vertical reduction coefficient is 0.96. The acting directions of the weights are also shown in Fig. 6 (CC Highway, 2015). Based on the analysis, the pressure generated by the RAB's vehicle load can be calculated as follows: $P^{\text{Pressure}}_{\text{Vehicle load}} = P_{\text{Vehicle load}}/S_{\text{Area}} \times \bigcup_{min}^{max}(r_{L1}\ ,\ r_{L2}) = 1660.196\ \text{N/m}^2$.

3.2.3. Flutter, buffeting, and wind load

The annual data on wind directions and climate and the surveys conducted in the typhoon season (Fig. 7) show that the prevailing wind directions throughout the year are northeast (45.57%) and northwest (25.47%). In the typhoon season (July–September), the prevailing wind directions are likewise northeast (47.63%) and northwest (25.01%). The general wind directions throughout the year are thus consistent with

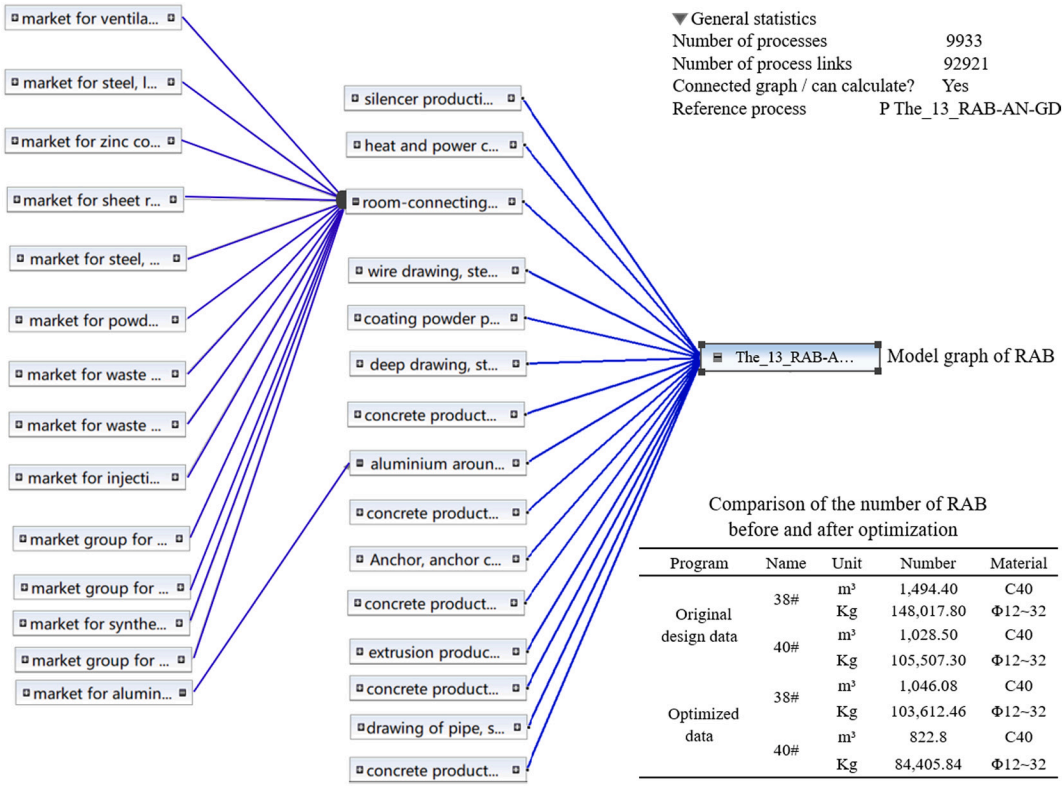

Fig. 16. Optimized structure position and change data and model graph of RAB.

Table 7
Comparison of RAB environmental impact data.

Material name	Number (t)	GWP	AP	FEP	PMFP	W
Original design emissions (kg)						
Concrete	8922.23	8,208,453.44	2230.56	12,758.79	18,022.91	30.60
	Transport	21,447.03	0.40	0.13	0.27	0.34
Steel	142.26	638,838.72	6515.59	4042.21	22,331.09	36,464.69
	Transport	287.28	0.01	0.00	0.00	0.00
Laboure consumption	Days	255.32	0.00	3.12	0.00	12.00
TO design emissions (kg)						
Concrete	8922.23	6,156,340.08	1672.92	9569.09	13,517.18	22.95
	Transport	16,085.27	0.30	0.10	0.20	0.26
Steel	142.26	479,129.04	4886.69	3031.66	16,748.32	27,348.52
	Transport	215.46	0.00	0.00	0.00	0.00
Laboure consumption	Days	191.49	0.00	2.34	0.00	9.00

those in the typhoon season. For the dynamic wind loads in this study, the northeast and northwest are the two prevailing wind directions to consider, with maximum wind speeds of 2.76 m/s and 3.37 m/s.

The two values are calculated in accordance with JTG/T 3360-01-2018 Wind-resistant Design Specification for Highway Bridges (Tongji University, 2018):

(1) Equivalent static gust load on the main beam:

$$F_g = \frac{1}{2}\rho U_g^2 C_H D \tag{23}$$

where F_g is the downwind equivalent static gust load acting on the unit length of the main beams (N/m); ρ is the air density with the value of 1.25 kg/m^3; U_g is the wind speed of the equivalent static gust (m/s); C_H is the cornering ratio of the main beam; D is the featured height of the main beam (m).

(2) Equivalent gust loads on piers, pylons, stay cables, and main cables:

$$F_g = \frac{1}{2}\rho U_g^2 C_D A_n \tag{24}$$

Where F_g is the wind load acting on the unit length of members (N/m); ρ is the air density with the value of 1.25 kg/m^3; U_g is the wind speed of the equivalent static gust on the reference height of the members (m/s); C_D is the frag coefficient of the members; A_n is the downwind projected area per unit length of the members (m^2/m), and this value of the stay cable or main cable is calculated based on the outer diameter.

The gust load of the main beams can be calculated as follows using Eq. (23) and the data in Fig. 6: $F_g = \frac{1}{2} \times 1.25 \times 3.37^2 \times 0.979 \times 3.2 = 22.237$ N/m.

The downwind load of the piers and towers can be calculated as follows using Eq. (24) and the data in Fig. 7: $F_g = \frac{1}{2} \times 1.25 \times 3.37^2 \times 1.601 \times 9.59 = 109.98$ N/m.

Table 1
Theoretical models for typical TO of bridges.

Reference	Condition	Formula	Symbol
Bendsøe and Kikuchi (1988) (1)	Linear elastic structure optimization and homogenization calculation method.	$\begin{cases} max[(1-\zeta)\mu_k, 0] & \text{if } h_k D_k^{\eta} \le max[(1-\zeta)\mu_k, 0] \\ \mu_k D_k^{\eta} & \text{if } max[(1-\zeta)\mu_k, 0] \le h_k D_k^{\eta} \le min[(1+\zeta)\mu_k, 1] \\ min[(1+\zeta)\mu_k, 1] & \text{if } min[(1+\zeta)\mu_k, 1] \le h_k D_k^{\eta} \end{cases}$	η is a weighting factor, and ζ a move limit; μ is the density.
Kurian (2021) (2)	Topology optimization process of continuous reinforced concrete (RC) structure.	$\begin{cases} Minimize: C = F^T U \\ \text{Subject}: V^* - \sum_x x_e v_e = 0 \\ \alpha_e = -\frac{P}{x_e} x_e^p u_e^T k_0 u_e = p \frac{E_e}{x_e} \end{cases}$	Where C is the compliance; x_e is the design variable indicates the presence or absence of the element; V^*indicates the target volume; v^e is the elemental volume; F and U are the global force vector and displacement vector; and P is the penalty exponent; the term $x_e^p u_e^T k_o u_e$ is exactly the element strain energy.
Jewett and Carstensen (2019a, 2019b) (3)	Algorithm framework of bilinear hybrid mesh topology optimization method.	$\begin{cases} \frac{Minimize\, f(\rho_c, \rho_t, \sigma_c, \sigma_t) = F^T d}{\text{subject to } K(\rho_c, \rho_t, \sigma_c, \sigma_t) d - F = 0} \\ c(\rho_c, \rho_t) = \sum_{e \in \Omega_c} \rho_c^e v_c^e + \sum_{e \in \Omega_t} \rho_t^e v_t^e - V \le 0 \\ \Phi_{\min} \le \Phi_i \le \Phi_{\max} \forall i \in \Omega \\ \frac{\partial f}{\partial \rho_c^e} = -\eta (\rho_c^e)^{\eta - 1} (d^e)^T K_{o,c}^e d^e \end{cases}$	Where Φ_i are the design variables that control the element densities in ρ;The assembly of a new stress-dependent global stiffness matrix $K(\rho_c, \rho_t, \sigma_c, \sigma_t)$.
Meng et al. (2020) (4)	Renewal formula of continuous discrete variables.	$\begin{cases} \text{Arg } min\, f(u, \rho), \rho = (\rho_1, \rho_2, \cdots, \rho_N) \\ s.t. 0 < \rho_i \le 1, i = 1, 2, \cdots, N \\ g_{j(\rho)} \le 0, j = 1, 2, \cdots, M \\ GU = F^a + F^{th} \text{ (Thermal coupling)} \end{cases}$	The penalization parameter ρ; Pseudo-density variable ρ_i; G is the global stiffness matrix; U the nodal displacement vector; F^a and F^{th} correspond to the equivalent force and thermal load vectors.
Zhang and Sun (2006) (5)	Homogeneous body, discrete as finite element model.	$\begin{cases} Min\Phi = -\sum_{i=1}^{m} U_i^T K_i(y_i) U_i \sum_{j=1}^{n} v_{i,j}^0 y_{ij} \le v_i^0 x_i, i = 1, m\, p(y_i) = \end{cases}$	Where$U_i$corresponds to the known nodal displacement vector of DE_iin the macroscale; $y_{i,j}$ and $v_{i,j}^0$ are the microscale density design variable and element volume associated with finite element j involved in DE_i; $C_{i,j}$ denote the strain energy and nodal displacement vector of finite element included in j density variable i.

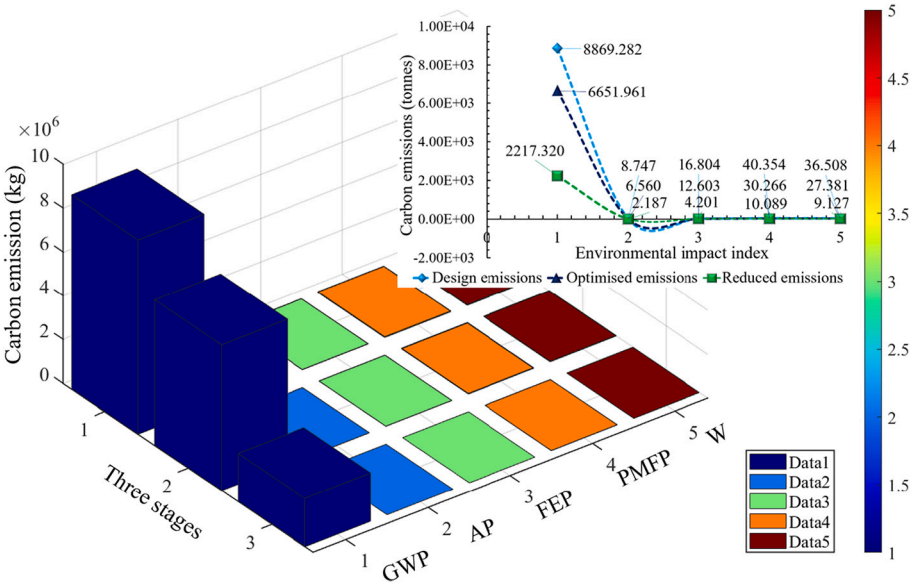

Fig. 17. Data comparison of environmental impact optimization on piers 39 and 40.

The downwind loads of the stay cables and main cables $F_g = \frac{1}{2} \times 1.25 \times 3.37^2 \times 1.601 \times 0.424 = 4.82$ N/m.

(3) Analysis of flutter force and buffeting force

The maximum wind speed of the designed bridge within 100 years is 36.8 m/s, which is much lower than the critical wind speed. According to the research data of Bin Jian (Jian et al., 2020), the buffeting displacement of the main bridge and the central tower is more significant in the standard wind spectrum and wind tunnel measurement. The wind speed and displacement data in three directions are obtained. The maximum wind speed in this paper is 36.8 m/s. Therefore, the displacement data corresponding to the top wind speed of 40 m/s is selected for analysis: the mid-span of the main beam (the most affected

area) $L_b = 0.115$ m, $D_b = 0.008$ m, $M_b = 0.052$ m; the top of the central tower (the most affected area) $L_h = 0.007{,}6$ m, $D_v = 0.028$ m.

RAB has set up longitudinal viscous dampers (model: DAMP-HX1–3) and transverse viscous dampers (model: DAMP-ZX) in the design scheme. The bridge design uses nonlinear viscous dampers. Eight groups (39#) are installed at the connection between the central tower and the main beam, and twelve groups (4 groups/pier) are established at the relationship between the 38#, 40#, and 41# piers and the main beam. Wang et al. (Wang et al., 2005) studied and determined the damping parameters and the maximum displacement of the double-tower cable-stayed bridge using the nonlinear dynamic time history analysis method.

According to the research conclusions of Wang and the analysis of the mechanical characteristics of the viscous damper designed by the case, it is determined that (Fig. 4): When C is 20,000 (damping coefficient), α is 1.0 (damping index), the maximum displacement of the top of the tower is 0.345 m, the relative displacement between the tower and the main beam is 0.326 m, the relative displacement between the main beam and 40# is 0.324 m, the main beam, and 39# And 41# relative displacement are 0.267 m. Damper damping force F is 15,680 KN (theoretical formula F is $C \times V^{\alpha}$, V = relative velocity (m/s)). Comparing the above analysis data, the authors show that the damper settings fully satisfy the dynamic response of wind loads and the seismic performance of the bridge.

The above analysis proves that 3.2.3's analysis process and the conclusion fully consider the dynamic performance of wind load (static wind speed, galloping vibration, flutter, and buffeting vibration).

3.2.4. Temperature stress

The highest temperature in a year is 28 °C, and the extreme maximum temperature is 37.2 °C (in 1978, which can be ignored). The annual average temperature is 18 °C; the lowest average temperature is 7.7 °C; the extreme minimum temperature is - 4.3 °C (in 1967, which can be ignored). The impact of temperature is divided into five intervals in the process of the primary bridge analysis: 5 °C ~ 10 °C ~ 15 °C ~ 20 °C ~ 25 °C ~ 30 °C. Since the relative stiffness of all parts of the bridge is changed due to the impact of air temperature variation on the concrete's Young's modulus, the changes in the stress and Young's modulus caused by temperature variations are considered (OBrien et al., 2020).

Table 4 shows the values of the compressive strength, elastic modulus, and Poisson's ratio of RAB's members under different temperatures.

3.3. Finite element model

A 3D solid model of RAB is built-in Abaqus, and a complete step and 9,641,110 elements are created in the model. The fine mesh is essential for the convergence of simulation results. But fine meshes of different sizes are adopted in each structural unit due to RAB's complex structures (Table 3), making the numerical convergence of the model tend to multiple elements of stable unique values (Al-Rousan, 2019).

Fig. 8 shows RAB's vibration mode and internal force distribution under the combined load (2) (maximum elements). It can be preliminarily estimated that RAB's maximum distortion appears on the main beam, the central tower, and stay cables. Establishing a 3D solid finite element model of large bridges is the first difficulty in this field of research: many researchers use the plate, shell, and rod elements instead of solid main beams, main towers, and stay cables, and simplify high-order and high-dimensional elements into two. Two orders reduce the difficulty of grid boundary division, data discretization accuracy, and research robustness, and it is challenging to realize single lattice research.

3.3.1. Analysis data of RAB

Under the action of the combined load, RAB is observed with apparent displacements during the loading. The Abaqus software is used to adjust the scale factor of vibration displacement to 1:12. In this way, the vibration mode and the changing responses of various bridge parts can be clearly observed.

Fig. 9a is the distribution of four types of parameters of the main beam, and 79 sets of measuring points are monitored, all of which are valid measuring points. The top five measuring points of each type are strain: 4664 (0.161) > 5462 (0.108) > 6474 (0.094) > 6466 (0.050) > 6464 (0.029). The positions of the five measuring points are all concentrated at the consolidation of the main beam, the central tower, and the main pier. The data proves that no support is set at the position of the cable tower. At the same time, stress and strain are concentrated in this area (the weakest part of the cable-stayed bridge structure). Stress: 6474 (275,517.0 Pa) > 6466 (211,866.0 Pa) > 5461 (119,632.0 Pa) > 6464 (96,816.7 Pa) > 12,379 (79,246.1 Pa). See Fig. 11 for the specific locations.

Displacement:12325 (1.162 m) > 12,395 (1.159 m) > 50,982 (1.100 m) > 50,128 (1.041 m) > 50,123 (1.031 m). The maximum displacement is at the middle position of the 83.94 m main beams in the direction of 38# → 39# (about 1/3 of the length of 38# ~ 39#). Under the action of multiple loads, the bending moment at the mid-span position of the cable-stayed bridge is not necessarily the largest. The other four groups of measuring points are distributed around the mid-span of 39# ~ 40#. Energy density: 4664 (227,323.5 J/m^3) > 6466 (23,826.94 J/m^3) > 6629 (20,764.94 J/m^3) > 6474 (20,403.21 J/m^3) > 6963 (11,152.85 J/m^3).This data represents how much energy is contained in a unit volume. The five sets of data are consistent with stress.

Fig. 9b data analysis of the central tower, a crucial stress-bearing structure of the cable-stayed bridge, monitored 77 sets of measuring points. The data are strain, 5463 (0.022) > 6632 (0.011) > 6631 (0.008) > 10,538 (0.008) > 5267 (0.005). The analysis conclusion is consistent with the main beam, and all focus on the main beam, tower, and pier consolidation; comparing the first five sets of strain data between the main beam and the tower, it is found that, S_{Girder}: S_{Tower}=8.11:1.00. The strain concentration of the main beam is much larger than that of the central tower. Stress: 4664 (453,672.5 Pa) > 5463 (106,762.4 Pa) > 4622 (80,354.5 Pa) > 6632 (71,702.5 Pa) > 6631 (58,230.5 Pa). The stress distribution position of the central tower is consistent with that of the main beam, and the two data are equal (the ratio is 1.02).

Displacement:4622 (1.931 m) > 5463 (1.695 m) > 4007 (1.441 m) > 3050 (1.277 m) > 4664 (1.135 m). We were comparing the data, and it was found that the displacement of the central tower is more significant than that of the main beam. The area is concentrated between the cap and the main beam. Energy density: 6971 (0.2937 J/m^3) > 12,720 (0.284 J/m^3) > 6659 (0.261 J/m^3) > 6968 (0.240 J/m^3) > 6472 (0.1712 J/m^3). The analysis results show that concentrated in the same position (consolidation), the energy per unit volume of the central tower is lower, and the data is close to zero.

Fig. 9c shows 95 sets of monitoring points for the stay cable, and the data are: strain: 5087 (0.048) > 5147 (0.038) > 5514 (0.037) > 5122 (0.037) > 5092 (0.035). Among the five sets of data, four sets of stay cables are located at the mid-span positions of 38# ~ 39# ~ 41#, which are consistent with the maximum displacement of the main beam. Stress: 5092 (204,586.86 Pa) > 5087 (175,434.02 Pa) > 5126 (173,999.23 Pa) > 5217 (160,018.70 Pa) > 5147 (142,925.88 Pa). The five groups of sets are all concentrated in the middle and sides of the 38# ~ 39# span.

Displacement:5217 (6.335 m) > 5748 (4.384 m) > 5389 (4.314 m) > 5147 (4.014 m) > 5052(3.891 m). The maximum displacement is on the R36 stay cable, and the 5087 is on the R18 stay cable (38# ~ 39# mid-span). The displacement of the stay cable is the largest among the components. During the maintenance period, the fatigue and aging damage of the stay cable should be strictly checked. Energy density: 5182 (1.117 J/m^3) > 5126 (1.112 J/m^3) > 5224 (1.111 J/m^3) > 5113 (1.091 J/m^3) > 5688 (1.086 J/m^3).

An abrupt change is detected from stress 2278 and stress 5625. The two points are located above support 40. The stay cables (made of elastoplastic materials) bear external load actions during the loading, resulting in a rapid increase of stress. The bearing capacity of the support

40 also increased, resulting in continuous fluctuations of the stress of the stay cables, as shown in Fig. 9c.

Fig. 9d sets 44 sets of monitoring points for piers 38#, 40# and 41#, and the data are: strain: 2568 (0.060) > 4985 (0.013) > 4973 (0.012) > 6959 (0.011) > 761 (0.011). 2568 is at the support position of the 38# pier, and the other three points are at the 41# pier. Stress: 2568 (258,220.80 Pa) > 6959 (159,557.89 Pa) > 4159 (142,913.41 Pa) > 2499 (115,392.09 Pa) > 2470 (106,970.04 Pa). The position of the first group of points is determined, and the other three groups are in the 40# pier.

Displacement: 4159 (1.081 m) > 2568 (1.057 m) > 6959 (0.893 m) > 2499 (0.225 m) > 2470 (0.209 m). The first two groups are on the top of the 38# pier; the other three are on the top of the 40# pier. Energy density: 6959 (0.639 J/m^3) > 2470 (0.560 J/m^3) > 2468 (0.544 J/m^3) > 9470 (0.524 J/m^3) > 2499 (0.479 J/m^3). The five groups of points are all in the 40# pier; the data is small and relatively concentrated.

Fig. 10a and b show the towers'consolidation area, beams and the area where the stress is concentrated. The maximum concentrated stress is 890,650 Pa (located at the consolidation area of the towers and beams on the left side of the 39 main towers). The node is also the maximum stress action point of the entire RAB.

Fig. 11 is the stress gradient of the 39 central tower, showing an inverted trapezoidal profile. The minimum stress of the cable tower above 100 m is 122.3 Pa.

Table 5 and Fig. 11 show the computational analysis results and data statistics of the finite element model. The RAB's stress and energy are concentrated on the 39 main tower and the 38–41 main beams and stay cables.

According to the research data provided in Figs. 9–11 and Table 5, the parts with less stress and displacement are concentrated on the lower part of 38, 40, and 41, so TO for these parts is conducted over two times. No optimization is performed for the pile foundation because it bears complex actions from geology and lithology (Mohamad et al., 2021). Other stress concentrations, large displacement, and deformation of members have been optimized in the original design, so they will not be analysed again.

3.3.2. Sensitivity

The sensitivities of all parts of RAB under the load action are analysed based on Eqs. (10) and (11), and the parts are divided as shown in Table 5.

The main beam sensitivity can be expressed as $\{\sigma\}^k = [R]^k[G]^k\{d\}^k$, where $\{d\}^k$ is the time corresponding to the stress frame number; $[R]^k$ is the stress matrix; and $[G]^k$ is the corresponding displacement matrix. To enhance the accuracy of the analysis, the top 12 groups of node stress and displacement are selected for each member (calculation example: main beam).

$[R]^k$, $[G]^k$, $\{d\}^k$, $\{\sigma\}^k$, $\sum\sigma^k$ (determined after data analysis and calculation). The remaining RAB parts are calculated in the same way (the calculation and analysis process is omitted).

$$\sum\sigma^e_{Max}=\left\{ \{\sigma\}^{e1}_{Girder\ max}\right.$$

$\{\sigma\}^{e2}_{38-39\ \text{Stay cable}\ max}\{\sigma\}^{e3}_{39-41\text{Stay cable}\ max}\{\sigma\}^{e4}_{38\text{Pier}\ max}$
$\{\sigma\}^{e5}_{39\text{Pier}\ max}\{\sigma\}^{e6}_{40\text{Pier}\ max}\{\sigma\}^{e7}_{41\ \text{Pier}\ max}25,517.00$
Pa175, 434.00 Pa145, 364.7 Pa

241, 129.80 Pa63, 152.98 Pa244, 960.22 Pa240, 974.00 Pa

$$\sum v_o{}^*=\left\{ \{v\}^{*1}_{\text{Girder O}\ max} \quad \{v\}^{*2}_{38-39\ \text{Stay cable O}\ max}\right.$$

$\{v\}^{*3}_{39-41\text{Stay cable O}\ max}\{v\}^{*4}_{38\ \text{Pier O}\ max}\ \{v\}^{*5}_{39\ \text{Pier O}\ max}$
$\{v\}^{*6}_{40\ \text{Pier O}\ max}\{v\}^{*7}_{41\ \text{Pier O}\ max}$0.786 m1.098 m1.070 m0.479 m

0.288 m0.656 m0.399 m

The high-order matrix multiplication is calculated by the Matlab software programming (Mathworks, 2021) in order to ensure the computational accuracy. The value ranges of $\{\sigma\}^k$ are shown as follows: 4510–750,330 for $\{\sigma\}^{k1}_{\text{Girder}}$; 11,800–1,816,000 for $\{\sigma\}^{k2}_{38-39\ \text{Stay cable}}$; 57,000–1,002,500 for $\{\sigma\}^{k3}_{39-41\ \text{Stay cable}}$; 1760–377,500 for $\{\sigma\}^{k4}_{38\ \text{Pier}}$; 239–14,441 for $\{\sigma\}^{k5}_{39\ \text{Pier}}$; 133–85,486 for $\{\sigma\}^{k6}_{40\ \text{Pier}}$; 29–42,443 for $\{\sigma\}_{41\ \text{Pier}}{}^{k7}$ (Unit: Pa/m·s).

3.3.3. Curve fitting approximation analysis

According to the criteria of displacement, stress, and sensitivity data, in order to avoid falling into local optimum and better solve the relationship between randomness parameters and diversity and convergence, the diversity data is transformed into a suitable measure related to the performance of the scientific algorithm. The swarm intelligence optimization algorithm is more complex than the actual stress situation. Set up an algorithm calling program (example: main beam) (Rostami et al., 2021).

>>x = [4477.726676.06 Same as Section 3.3.2 data ⋯ 10,739.33119631.6211495.46 ⋯ 79,246.08];

>>y = [0.004 0.001 0.004 0.008 Same as Section 3.3.2 data ⋯0.292 0.154 0.341 ⋯ 0.565];

>>Plot (x, y,'*'); P = polyfit (x, y, 3); plot (x, y,'*', x, polyval (p, x)).

According to the above algorithm, the optimal curve fitting and steer distribution of the main girder can be obtained.

Fig. 12a shows the 38 pier of linear model polynomial fit with 95% confidence bounds; SSE (goodness of fit): 0.373, R-square: 0.691. The fitting conclusion is accurate (there are 39.4% redundant structures and discrete elements).

Fig. 12b shows the 39 pier of linear model polynomial fit with 95% confidence bounds; SSE: 0.125, R-square: 0.813. The fitting conclusion is accurate (there are 8.33% redundant structures and discrete elements).

Fig. 12c shows the 40 pier of linear model polynomial fit with 95% confidence bounds; SSE: 0.545, R-square: 0.815. The fitting conclusion is basically accurate (there are 29.63% redundant structures and discrete elements).

Fig. 12d shows the 41 pier of linear model polynomial fit with 95% confidence bounds; SSE: 0.275, R-square: 0.819. The fitting conclusion is accurate (there are 34.72% redundant structures and discrete elements).

Fig. 12e shows the girder of locally weighted smoothing linear regression fit, $f(x, y)$ = linear smoothing regression computed from p. SSE: 0.037, R-square: 0.868. The fitting conclusion is very accurate (there are 12.9% redundant structures and discrete elements).

Fig. 12f shows the thin-plate spline interpolant fit's 38–39 stay cable. $f(x, y)$ = thin-plate spline computed from p. SSE: 5.345e-20, R-square: 1. The fitting conclusion is the bigger accuracy (there are no redundant structures and discrete elements).

Fig.12g shows the 39–41 stay cable of linear model polynomial fit with 95% confidence bounds; SSE: 0.161, R-square: 0.991. The fitting conclusion is accurate (there are no redundant structures and discrete elements).

Fig. 12a, c, and d show high dispersion; the dispersion samples have large, unstable jumps and redundant elements. There is no regular distribution between the optimal 3D curve and the scattered points, and it has multiple optimization topology conditions. Fig. 12b, e, f, g the scattered samples are distributed on or near the two sides of the fitting surface, and there is no high dispersion phenomenon.

3.3.4. Topology optimization

The stress and displacement are used to discretise the structure into dense finite element meshes. Within the defined range of the original load constraints, the unit elements that satisfy the minimum principal stress are designed, and the sensitivity $\{\sigma\}^k$ is judged for such unit elements. The low-stress units are deleted after the above flow, and the maximum bearing capacity and deflection of the remaining RAB parts

should also be kept within the specifications.

The setting of performance index parameters: 38–41 bent caps and pier studs; the pier base is an RC compressed structure. After the optimization design, $|\sigma^e_{max}| < |\sigma_{Design}{}^*|$ (I.e., the maximum principal stress limit after optimization < the specified stress limits) will be realised. At the same time, the stress constraints are proportioned for RAB's volume after the optimization design, which can be expressed as $v_o{}^* = (|\sigma^e_{max}|/|\sigma_{Design}{}^*|)v_d{}^*$ (where $v_o{}^*$ is the optimized volume; $v_d{}^*$ is the original volume).

The validity of the TO is verified by control index parameters such as $\{\sigma\}^k$, σ^e_{max} and $v_o{}^*$.

Structural TOs for Pier 38, Pier 40, and Pier 41:

After the stress, displacement, and sensitivity of each part of RAB are determined in Sections 3.3.1 and 3.3.2, the structural TOs are conducted for Piers 38, 40, and 41. Under the conditions described in Section 3.2, when several iterative steps have been carried out on the structure, the three indexes $\{\sigma\}^k$, σ^e_{max} and $v_o{}^*$ determine the final convergence stability value and the optimal structure.

Fig. 13a shows that Pier 38 undergoes TO three times under the original load action, and the $\{\sigma\}^k$, σ^e_{max} and $v_o{}^*$ are analysed three times, finding that the second time is the most reasonable optimization. The optimization is finished after 13 iterations; the structural volume drops by 30% (the remaining part is equivalent to 70% of the original volume). The author detected maximum stress (51,521.40 Pa: Stress distribution data of 38 pier in the structure after volume reduction;) is concentrated on the contact of the right pier base with the pier stud (element no. 611). The changes to the displacement and stress are shown in Fig. 13b.

As shown in Fig. 14a, Pier 40 undergoes TO four times under the original load action. The $\{\sigma\}^k$, σ^e_{max} and $v_o{}^*$ are analysed four times, finding that the third time is the most reasonable optimization. The optimization is finished after 13 iterations; the structural volume drops by 20%, and the remaining part is equivalent to 80% of the original volume. The maximum stress (31,365.69 Pa) is concentrated on the top contact on the right pier stud (element no. 65). The changes to the displacement and stress are shown in Fig. 14b.

As shown in Fig. 15, Pier 41 undergoes TO five times under the original load action. The $\{\sigma\}^k$, σ^e_{max} and $v_o{}^*$ are compared five times, finding that all of them are higher than the standard value in Section 3.3, so it cannot be subject to TO again. The data are shown in Table 6.

4. Analysis of LCA

The research conclusions in Section 3.3.3 indicate that pier 38 and pier 40 meet the research conditions for environmental sustainability, so that the environmental impact analysis can be further conducted. The carbon emissions of the original structures are mainly from the production and transportation of concrete and steel.

The design phase LCA emissions analysis principles are defined in Section 2.5. According to the original design drawings, determine the increase or decrease of pier 38 and pier40 materials. Software analysis: Import the original design materials, personnel, and machinery. The optimized materials, personnel, and machinery into the open LCA software analysis system. The analysis steps are import data into the Processes system → apply and analyse through the database of product systems, → generate a model graph, and statistics →generate results of the project (Fig. 16). The entire data access analysis is completed, and the system uses Monte Carlo simulation algorithm to deal with the disturbance of uncertain factors.

Ten categories of impact factor data are generated in the LCA analysis report. Five categories are selected as the basis for analysis in Section 2.5.1 for factors closely related to this study. The original design 38# and 40# concrete and steel consumption are 1494.4m^3, 1028.5m^3, 148,017.8 kg, and 105,507.3 kg, respectively. After optimization, they are reduced by 448.32 m^3, 205.70 m^3, 44,405.34 kg, and 21,101.46 kg, respectively. The labour and equipment follow the original design. The protocol was scaled down (Fig. 16).

As shown in Table 7, The total emissions of environmental pollution of the original forms are 8971.69 t. The consumption of raw materials for Pier 38 is reduced by 30%, and for Pier 40 by 20%. The carbon emissions of the raw materials are reduced by 2242.92 t.

It can be seen from Fig. 17 that the RAB's GWP reduced by 2217.32 t after TO, accounting for 98.9% of the total reductions and 33.3% of the total emissions. This is a significant and efficient reduction of the carbon emissions of raw materials.

It is found from the study on the TOs of Pier 38, Pier 40, and Pier 41 that $\{\sigma\}^k$, σ^e_{max} and $v_o{}^*$ are the critical control indexes of optimization in the modeling data analysis of the entire bridge. In the optimization process of Pier 41, some values exceed the specifications, and the specific reasons will be explored in future studies.

5. Conclusion

In order to reduce the emissions of environmental pollution of bridges in the building industry, the modeling and case analysis methods are used in this paper. The RAB's carbon emissions reduce by 2242.92 t, which is a stunning figure. The results remind designers TO carry out multiple times of optimization analysis for buildings.

Based on modeling and data analysis, this research conducted a comprehensive research analysis and applied the robustness of constant dynamic load. Emphasis is placed on the effects of variable vehicles and temperature stress, which are rare in the researching complex 3D solid structures in static and dynamic environments. In the later data analysis, various mathematical research models are used to solve the diversity and convergence of the data. It provides effective theoretical research methods and data for the static and dynamic control and response design of bridges in the future.

The relevant analysis process and theoretical data are valid, reflecting the superiority of the optimal TO, and providing references for the optimization of similar bridge structures. There are also some deficiencies in this study because no further verification and analysis is conducted on whether the optimized facilities of Pier 38 and Pier 40 can meet the conditions of site construction. The uninvolved matters also include whether there are difficulties in formwork processing and concrete pouring for the optimized structures.

The scientific analysis method of higher mathematics is an effective means to solve discrete problems. This paper studies and establishes the curve-fitting mathematical model of swarm intelligence optimization algorithm, which solves the problem of diversity and convergence data. The results are consistent with the sensitivity analysis.

Further research work can be carried out from perspectives such as the application and sustainable development of bridge structures' TOs in international engineering projects, how to combine the TO and sustainable development of new and existing bridge structures in the world, and the optimal optimization of carbon emissions and natural environment of regional bridge structures.

CRediT authorship contribution statement

Zhi Wu Zhou: Conceptualization, Methodology, Software, Formal analysis, Investigation, Data curation, Writing – original draft. **Julián Alcalá:** Conceptualization, Validation, Formal analysis, Resources, Writing – review & editing, Project administration. **Víctor Yepes:** Conceptualization, Validation, Resources, Writing – review & editing, Supervision, Funding acquisition.

Declaration of Competing Interest

The authors declare that they have no known competing financial interests or personal relationships that could have appeared to influence the work reported in this paper.

Acknowledgements

The authors gratefully acknowledge the funding received from the following research projects: Grant PID2020-117056RB-I00 funded by MCIN/AEI/10.13039/501100011033 and by "ERDF A way of making Europe".

References

Aigbavboa, C., Ohiomah, I., Zwane, T., 2017. Sustainable construction practices: "a Lazy View" of construction professionals in the South Africa construction industry. In: Energy Procedia. Elsevier Ltd, pp. 3003–3010. https://doi.org/10.1016/j.egypro.2017.03.743.

Allaire, G., Jouve, F., Maillot, H., 2004. Topology optimization for minimum stress design with the homogenization method. Struct. Multidiscip. Optim. 28, 87–98. https://doi.org/10.1007/s00158-004-0442-8.

Al-Rousan, R., 2019. The impact of cable spacing on the behavior of cable-stayed bridges. Mag. Civil Eng. 49–59. https://doi.org/10.18720/MCE.91.5.

Bajželj, B., Allwood, J.M., Cullen, J.M., 2013. Designing climate change mitigation plans that add up. Environ. Sci. Technol. 47, 8062–8069. https://doi.org/10.1021/es400399h.

Bendsøe, M.P., Kikuchi, N., 1988. Generating optimal topologies in structural design using a homogenization method. Comput. Methods Appl. Mech. Eng. 71, 197–224. https://doi.org/10.1016/0045-7825(88)90086-2.

CC Highway Consultants Co., L., 2015. General Specifications for Design of Highway Bridges and Culverts. Minitry Transp. People's Repub. China. http://xxgk.mot.gov.cn/2020/jigou/glj/202006/t20200623_3312312.html.

Cid Montoya, M., Hernández, S., Nieto, F., 2018. Shape optimization of streamlined decks of cable-stayed bridges considering aeroelastic and structural constraints. J. Wind Eng. Ind. Aerodyn. 177, 429–455. https://doi.org/10.1016/j.jweia.2017.12.018.

Cid Montoya, M., Nieto, F., Hernández, S., Fontán, A., Jurado, J.A., Kareem, A., 2021. Optimization of bridges with short gap streamlined twin-box decks considering structural, flutter and buffeting performance. J. Wind Eng. Ind. Aerodyn. 208, 104316 https://doi.org/10.1016/j.jweia.2020.104316.

Davenport, A.G., 1962. Buffetting of a suspension bridge by storm winds. J. Struct. Div. 88, 233–270. https://doi.org/10.1061/JSDEAG.0000773.

Ek, K., Mathern, A., Rempling, R., Brinkhoff, P., Karlsson, M., Norin, M., 2020. Life cycle sustainability performance assessment method for comparison of civil engineering works design concepts: case study of a bridge. Int. J. Environ. Res. Public Health 17, 7909. https://doi.org/10.3390/ijerph17217909.

Feng, Y., Lan, C., Briseghella, B., Fenu, L., Zordan, T., 2020. Cable optimization of a cable-stayed bridge based on genetic algorithms and the influence matrix method. Eng. Optim. 1–20. https://doi.org/10.1080/0305215X.2020.1850709.

García-Segura, T., Yepes, V., Frangopol, D.M., 2017. Multi-objective design of post-tensioned concrete road bridges using artificial neural networks. Struct. Multidiscip. Optim. 56, 139–150. https://doi.org/10.1007/s00158-017-1653-0.

Goverse, T., Hekkert, M.P., Groenewegen, P., Worrell, E., Smits, R.E.H.M., 2001. Wood innovation in the residential construction sector; opportunities and constraints. Resour. Conserv. Recycl. 34, 53–74. https://doi.org/10.1016/S0921-3449(01)00093-3.

Guide, T.T., 2017. The Pouring of the Beam on the Main Tower of the Feiyun River Cross-Sea Bridge Was Completed Smoothly. Zhejiang Prov. Dep. Transp.. http://jtyst.zj.gov.cn/art/2017/6/16/art_1676377_41155954.html

Guo, X., Zhang, C., Chen, Z., 2020. Dynamic performance and damage evaluation of a scoured double-pylon cable-stayed bridge under ship impact. Eng. Struct. 216, 110772 https://doi.org/10.1016/j.engstruct.2020.110772.

Hu, F., Lu, Y., Zhang, X., Zhang, Y., 2019. General design and key technology of Nanchang Chaoyang Bridge. Struct. Eng. Int. 29, 319–325. https://doi.org/10.1080/10168664.2018.1549466.

Jewett, J.L., Carstensen, J.V., 2019a. Experimental investigation of strut-and-tie layouts in deep RC beams designed with hybrid bi-linear topology optimization. Eng. Struct. 197 https://doi.org/10.1016/j.engstruct.2019.109322.

Jewett, J.L., Carstensen, J.V., 2019b. Topology-optimized design, construction and experimental evaluation of concrete beams. Autom. Constr. 102, 59–67. https://doi.org/10.1016/j.autcon.2019.02.001.

Jian, B., Su, Y., Li, M., 2020. Buffeting response of cable-stayed bridge during construction under skew winds and pylon interference. KSCE J. Civ. Eng. 24, 2971–2979. https://doi.org/10.1007/s12205-020-1822-3.

Kobayashi, G., Roh, T., Lee, J., Choi, T., 2020. Flexible Bayesian quantile curve fitting with shape restrictions under the Dirichlet process mixture of the generalized asymmetric Laplace distribution. Can. J. Stat. https://doi.org/10.1002/cjs.11582 cjs.11582.

Kurian, R.M.S.P.S., 2021. Advances in Civil Engineering, Lecture Notes in Civil Engineering. Springer Singapore, Singapore. https://doi.org/10.1007/978-981-15-5644-9.

Li, K., Zhao, L., Ge, Y.J., Guo, Z.W., 2017. Flutter suppression of a suspension bridge sectional model by the feedback controlled twin-winglet system. J. Wind Eng. Ind. Aerodyn. 168, 101–109. https://doi.org/10.1016/j.jweia.2017.05.007.

Malhotra, R., Khanna, M., Raje, R.R., 2017. On the application of search-based techniques for software engineering predictive modeling: a systematic review and future directions. Swarm Evol. Comput. 32, 85–109. https://doi.org/10.1016/j.swevo.2016.10.002.

Mao, J.-X., Wang, H., Feng, D.-M., Tao, T.-Y., Zheng, W.-Z., 2018. Investigation of dynamic properties of long-span cable-stayed bridges based on one-year monitoring data under normal operating condition. Struct. Control. Health Monit. 25, e2146 https://doi.org/10.1002/stc.2146.

Mathworks, 2021. Matlab and Training. Mathworks. https://matlabacademy.mathworks.com/?s_tid=pl_learn.

Meng, L., Zhang, W., Quan, D., Shi, G., Tang, L., Hou, Y., Breitkopf, P., Zhu, J., Gao, T., 2020. From Topology Optimization Design to Additive Manufacturing: Today's Success and Tomorrow's Roadmap. Arch. Comput. Methods Eng. 27, 805–830. https://doi.org/10.1007/s11831-019-09331-1.

Mohamad, Z., Fardoun, F., Meftah, F., 2021. A review on energy piles design, evaluation, and optimization. J. Clean. Prod. https://doi.org/10.1016/j.jclepro.2021.125802.

OBrien, E.J., Heitner, B., Žnidarič, A., Schoefs, F., Causse, G., Yalamas, T., 2020. Validation of bridge health monitoring system using temperature as a proxy for damage. Struct. Control. Health Monit. 27, 1–14. https://doi.org/10.1002/stc.2588.

Paya-Zaforteza, I., Yepes, V., González-Vidosa, F., Hospitaler, A., 2010. On the Weibull cost estimation of building frames designed by simulated annealing. Meccanica 45, 693–704. https://doi.org/10.1007/s11012-010-9285-0.

Penadés-Plà, V., Martínez-Muñoz, D., García-Segura, T., Navarro, I.J., Yepes, V., 2020. Environmental and social impact assessment of optimized post-tensioned concrete road bridges. Sustainability 12, 4265. https://doi.org/10.3390/su12104265.

Pons, J.J., Penadés-Plà, V., Yepes, V., Martí, J.V., 2018. Life cycle assessment of earth-retaining walls: an environmental comparison. J. Clean. Prod. 192, 411–420. https://doi.org/10.1016/j.jclepro.2018.04.268.

Rostami, M., Berahmand, K., Nasiri, E., Forouzandeh, S., 2021. Review of swarm intelligence-based feature selection methods. Eng. Appl. Artif. Intell. 100, 104210 https://doi.org/10.1016/j.engappai.2021.104210.

Sarkar, P.P., Jones, N.P., Scanlan, R.H., 1994. Identification of aeroelastic parameters of flexible bridges. J. Eng. Mech. 120, 1718–1742. https://doi.org/10.1061/(ASCE)0733-9399(1994)120:8(1718).

Secundo, G., Ndou, V., Del Vecchio, P., De Pascale, G., 2020. Sustainable development, intellectual capital and technology policies: a structured literature review and future research agenda. Technol. Forecast. Soc. Change 153, 119917. https://doi.org/10.1016/j.techfore.2020.119917.

Semenova, G., 2020. Global environmental problems in the world. E3S Web Conf. 217, 11004. https://doi.org/10.1051/e3sconf/202021711004.

Shao, X., Deng, F., Deng, L., 2018. Conceptual design of a new three-tower cable-stayed bridge system with unequal-size fans. J. Bridg. Eng. 23, 06018002. https://doi.org/10.1061/(ASCE)BE.1943-5592.0001257.

Tongjiuniversity, 2018. Wind-Resistant Design Specification for Highway Bridge. Tongjiuniversity. http://xxgk.mot.gov.cn/2020/jigou/glj/202006/t20200623_3313096.html.

Torres-Machí, C., Chamorro, A., Pellicer, E., Yepes, V., Videla, C., 2015. Sustainable Pavement Management. Transp. Res. Rec. J. Transp. Res. Board 2523, 56–63. https://doi.org/10.3141/2523-07.

Tsai, W.H., Lin, S.J., Liu, J.Y., Lin, W.R., Lee, K.C., 2011. Incorporating life cycle assessments into building project decision-making: an energy consumption and CO2 emission perspective. Energy 36, 3022–3029. https://doi.org/10.1016/j.energy.2011.02.046.

Wang, D., Gao, W., 2019. Robust topology optimization under load position uncertainty. Int. J. Numer. Methods Eng. 120, 1249–1272. https://doi.org/10.1002/nme.6180.

Wang, Z.Q., De Hu, S., Fan, L.C., 2005. Research on viscous damper parameters of Donghai bridge. Zhongguo Gonglu Xuebao/China J. Highw. Transp. 18, 37–42. http://zgglxb.chd.edu.cn/EN/abstract/abstract1031.shtml.

Wang, X., Wu, Z., Wu, G., Zhu, H., Zen, F., 2013. Enhancement of basalt FRP by hybridization for long-span cable-stayed bridge. Compos. Part B Eng. 44, 184–192. https://doi.org/10.1016/j.compositesb.2012.06.001.

Wang, H., Chen, C., Xing, C., Li, A., 2014. Influence of structural parameters on dynamic characteristics and wind-induced buffeting responses of a super-long-span cable-stayed bridge. Earthq. Eng. Eng. Vib. 13, 389–399. https://doi.org/10.1007/s11803-014-0250-0.

Yang, X., Hu, M., Wu, J., Zhao, B., 2018. Building-information-modeling enabled life cycle assessment, a case study on carbon footprint accounting for a residential building in China. J. Clean. Prod. 183, 729–743. https://doi.org/10.1016/j.jclepro.2018.02.070.

Zhang, W., Sun, S., 2006. Scale-related topology optimization of cellular materials and structures. Int. J. Numer. Methods Eng. 68, 993–1011. https://doi.org/10.1002/nme.1743.

Zhang, M., Li, Y., Wang, B., 2016. Effects of fundamental factors on coupled vibration of wind-rail vehicle-bridge system for long-span cable-stayed bridge. J. Cent. South Univ. 23, 1264–1272. https://doi.org/10.1007/s11771-016-0376-5.

Zhou, Z., Alcalá, J., Yepes, V., 2020a. Bridge carbon emissions and driving factors based on a life-cycle assessment case study: cable-stayed bridge over Hun he river in Liaoning, China. Int. J. Environ. Res. Public Health 17, 5953. https://doi.org/10.3390/ijerph17165953.

Zhou, Z., Alcalá, J., Yepes, V., 2020b. Environmental, economic and social impact assessment: study of bridges in China's five major economic regions. Int. J. Environ. Res. Public Health 18, 122. https://doi.org/10.3390/ijerph18010122.

Zhou, Z.W., Alcalá, J., Yepes, V., 2022. Regional sustainable development impact through sustainable bridge optimization. Structures 41, 1061–1076. https://doi.org/10.1016/j.istruc.2022.05.047.